AlbaEXP_PROJ_DOC_01.dotx

EXPERIMENTS DIVISION

9	Project	Created	Printed	Pages	Revision
001		2017-05-10		49	1.2
	XAIRA_OpticalDesign_1.2.docx				

Optical design of the XAIRA Beamline

Prepared by	Checked by	Approved by
J Juanhuix Gibert		

Distribution list

XAIRA board, Alfresco, team managers, Optical Review Panel Members

Document Change log

Author	Change Description	Date	Version
JJ	Start	10/05/2017	0.1
JJ	Major changes in optics	14/09/2017	0.2
JJ	Major changes in optics	11/11/2017	0.3
JJ	Added services, other OEs, etc	04/12/2017	0.5
JJ	Included input from NG, JN	04/12/2017	1.0
JJ	Recalculated thermal radii, updated table 8	11/12/2017	1.1

Contents

1 Introduction

1.1 Scientific case

This document reports the design of the optics for the BL06-XAIRA beamline at the ALBA Synchrotron light source. XAIRA will be a microfocus beamline dedicated to Macromolecular Crystallography (MX) experiments at ALBA, and will be complementary to the already existing MX beamline BL13-XALOC. It has been approved and funded as a Phase 3 beamline. The scientific case was presented by the MX Spanish community in 2014 during the selection process for the new Phase III beamlines, and approved later by the Alba council following the advice by the Scientific Advisory Committee.

It is difficult to emphasize the importance of having 3D structures at near atomic resolution structures of the macromolecules involved in any relevant biological function. MX has been for the last 30 years the most important high resolution method for the structural analysis of the biological macromolecules. The development of the synchrotron beamlines and the modern molecular-biology techniques has continuously improved synchrotron-based MX, which has been lately complemented with the XFEL-based MX [1] and, especially, the cryoelectron microscopy (CryoEM). As SR-MX has developed, the targets of structure analysis have evolved to be more challenging and scientifically important [2]. One of the principal difficulties in the use of SR-MX is undoubtedly obtaining crystals with a suitable size and sufficient diffracting power for useful MX data collection. The availability of MX microfocus beamlines, combined with workhorse beamlines, is therefore mandatory to fully exploit the potentiality of the technique. In response to this need, the BL06-XAIRA beamline is planned to tackle difficult MX experiments which may require a stable microfocus beam at a typical photon energy of 12.6 keV (~1 Å). The beamline has to offer a flexible sample environment set up and a user-friendly control system to allow performing smoothly most of the currently developing strategies for data collection [3].

At the same time, the native SAD phasing method, which profits from the anomalous scattering of light atoms present in crystals of native macromolecules is experiencing an increasing interest [4][5]. The typical elements naturally occurring in macromolecules (sodium, magnesium, phosphorus, sulfur, chlorine, potassium and calcium) have absorption K-edges in the range of 1-4 keV. Anomalous signal is thus higher in the lower limit of the photon energy range of the standard beamlines dedicated to MX. Besides, recent publications show that, at a given photon energy, the anomalous signal increases as the crystal is smaller [6]–[8]. This facts suggest that a microfocus beamline reaching relatively low energies, say, around 4-5 keV, would be ideal to exploit native phasing methods.

The growing interest for native phasing is revealed by the very recent implementation of an automated procedure to exploit the anomalous signal from iodine at the beamlines ID23-1 and ID23-2 at the ESRF [9]. The data collections at these beamlines are taken using a beam of a size of 10-50 μm and λ=1.85 Å (6.7 keV). Another initiative by PHENIX developers is also ongoing [10]. However, apart from the NYX initiative at the NSLS-II, to our knowledge no attempts have been made to optimize the entire beamline, including optics, to fully exploit the capabilities of native phasing. Therefore, the use of a microfocus (~1 μm beam size) beamline at very low energies (4-6 keV) constitutes an unexplored niche.

BL06-XAIRA aims at covering this niche. To this aim, the optical design extends the energy range to 4 keV in the low limit and reduces the beam air path and the use of windows along the beamline. Nevertheless, the design of the beamline instrumentation to implement the

native phasing at such low energies has to be always compatible with the main use of the beamline at 1 Å. A more specialized approach, such as that taken by beamline I23 at Diamond [11], is therefore disregarded.

1.2 Beamline summary

As required by the microfocus MX proposal in phase III and later confirmed by the ALBA SAC, the performance requirements for the beamline optics are summarized in Table 1. It is worth noting that the design of the beamline optics presented in the proposal could not be implemented, as the monochromator cannot withstand the power load from the undulator if placed as the first optical element.

Optical element		Value	Comments
Energy Range	keV	4 - 14	
Wavelength range	Å	3.1 - 0.885	
Beam size at sample (FWHM, h×v)	μm×μm	3×1	Full beam Variable size
Flux	ph/s	>2 10^{12}	At 12.661 keV. The source needs to be an ID.

Table 1. Basic performance requirements of the BL06-XAIRA beamline.

The optics layout as presented in this report is sketched in Figure 1, and the main parameters of the optical elements are listed in Table 2. Basically, the optics relies in the low divergence given by an undulator, a Si(111) crystal monochromator and meridionally-bent mechanical mirrors. The beamline is windowless, except at the end of the vacuum pipe at the sample position.

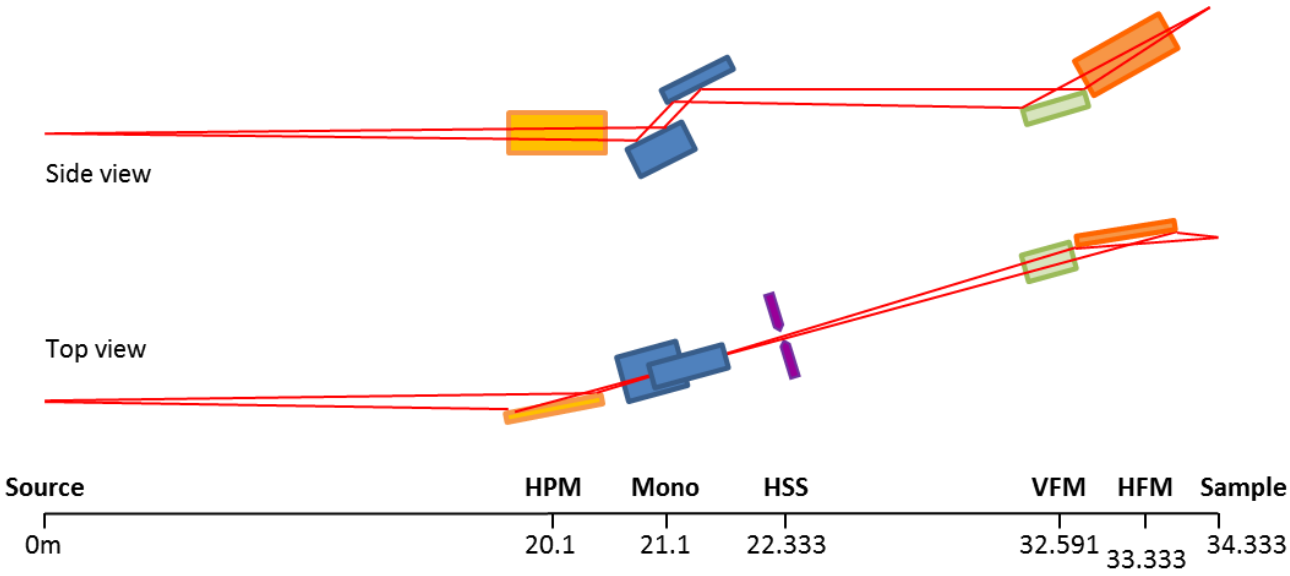

Figure 1. Sketch of the optical elements of BL06-XAIRA.

Optical element		Distance from source [m]	Characteristics
Moveable masks	MMK	13.7	Absorbing 3.04 kW
Horizontal Prefocusing Mirror	HPM	20.1	450 mm length Rh coated
Monochromator	Mono	21.1	Si(111) Multilayer Mo/B_4C 4.5 mm gap between crystals
Horizontal Secondary Slit	HSS	22.333	
Vertical Focusing Mirror	VFM	32.591	400 mm length Rh, Si stripes
Horizontal Focusing Mirror	HFM	33.333	800 mm length Rh, Si stripes
Sample position	Sam	34.333	

Table 2. Characteristics of the main optical components.

1.3 Credits

This document has been elaborated using data from the following Alba staff

- J. Juanhuix
- Josep Nicolás: ART raytracing program, mirror optimization, optical libraries and support.
- Nahikari González: Engineering design, and hutches lay out.
- Pep Campmany: ID calculations
- Jordi Marcos: Front end design
- Marcos Quispe, Liudmila Nikitina: FEA calculations
- Pablo Pedreira and Josep Nicolás: Beamline parameters and performances correlation matrix.
- Arnaud Devienne and Nahikari González: safety calculations

1.4 Heat load scenarios

With respect to the heat load absorbed by the optical elements, two scenarios have been consistently considered through the document.

- *Working conditions*: 250 mA at the storage ring (nominal current) and a front-end angular aperture of 0.35×0.15 mrad^2.

- *Worst conditions*: 400 mA at the storage ring (maximum design current) and a front-end angular aperture of 0.3×0.1 mrad^2.

The angular acceptances indicated above are needed to align the front end elements. The horizontal angular divergence is actually larger than acceptance of the beamline optics and is further reduced downstream the beamline to 0.1 mrad due to the limited acceptance of the horizontal prefocusing mirror (HPM). However, in operation conditions without misalignments the acceptances of the front end and the beamline optics should match.

2 Photon source

2.1 Design parameters

The photon source has to maximize the flux at a wavelength of 12.4 keV (~1 Å), as specified by the main scientific case. At the same time, it has to be fully tuneable from that energy down to 4 keV (~3.1 Å) to perform native phasing experiments at low energies (long wavelengths).

The source size is limited essentially by the emittance of the ALBA storage ring and the electron beam dimensions at the straight section where the undulator is installed. Therefore it is not part of the specifications of the source. The BL06-XAIRA beamline will use the port 06 of the ALBA storage ring, which corresponds to a mid-length straight section. The electron beam parameters of the straight section are listed in Table 3.

The photon source of the XAIRA beamline will be a planar in-vacuum undulator (IVU19). This type of source is the brightest available and gives the maximum flux in 3rd generation sources such Alba. The parameters of the ID are listed in Table 4. According to the magnetic array model, the peak magnetic field of the IVU19 is approximated to the phenomenological expression

$$B_0 = a\, e^{b\frac{g}{\lambda_U} + c\left(\frac{g}{\lambda_U}\right)^2} \qquad (1)$$

where g is the magnetic gap and a, b, and c are adjusting parameters, which for the IVU19 are adjusted to a = 2.89096 T, b = -3.6141 and c = 0.24739. The deflection parameter and beam properties can be derived from the expression above.

Straight section	Mid straight section/port 06	
Horizontal electron beam size (RMS)	x [μm]	130.44
Horizontal electron beam divergence (RMS)	x' [μrad]	46.88
Vertical electron beam size (RMS)	y [μm]	5.25
Vertical electron beam divergence (RMS)	y' [μrad]	4.34

Table 3. Parameters of the straight section selected to install the XAIRA insertion device.

ID characteristics		
Magnetic period [mm]	λ_U [mm]	19.9
Type of material		Hybrid, NdFeB
Maximum peak magnetic field	B_0 [T]	1.151
Deflection parameter	K [#]	2.14
ID length	L [m]	2.3
Number of periods	N_λ [#]	115

Table 4. Parameters of IVU19 and the characteristics of the delivered photon beam. The vertical beam size and divergence depend on the photon energy.

2.2 Photon beam characteristics

The beam source size and divergence as modelled using ART ray tracing program [12] are shown in Figure 2. The characteristics of the photon beam delivered by the IVU19 are listed in Table 5.

The photon beam size and divergence in the horizontal dimension are much larger than those in the vertical direction. This profile is characteristic from the insertion devices installed in 3rd and 4th generation synchrotron sources. The horizontal beam size and divergence do not change within the useful energy range of the beamline, whereas the vertical dimensions decrease slightly with the photon energy and the magnetic gap.

The undulator period and the possibility to reduce the magnetic gap down to only 5.2 mm allow the full tunability of the beamline in the designed spectral range 4-14 keV (Figure 3). Note that at the minimum magnetic gap, the 3rd harmonic falls at a photon energy 4 keV, whereas the 9th harmonic falls at 12 keV. This has been the optimal solution complying with the requirements from the scientific case.

Photon beam characteristics		
Beam size (h×v, FWHM)	Σ_x, Σ_y [μm]	307 × 14-20
Beam divergence (h×v, FWHM)	Σ'_x, Σ'_y [μrad]	111 × 29-34
Flux at 12.661 keV	F [ph/s/0.1%BW]	$1.65\ 10^{14}$
Total power at 400 mA in SR	P_T [kW]	6.9

Table 5. Characteristics of the photon beam delivered by the IVU19. The vertical beam size and divergence depend on the photon energy.

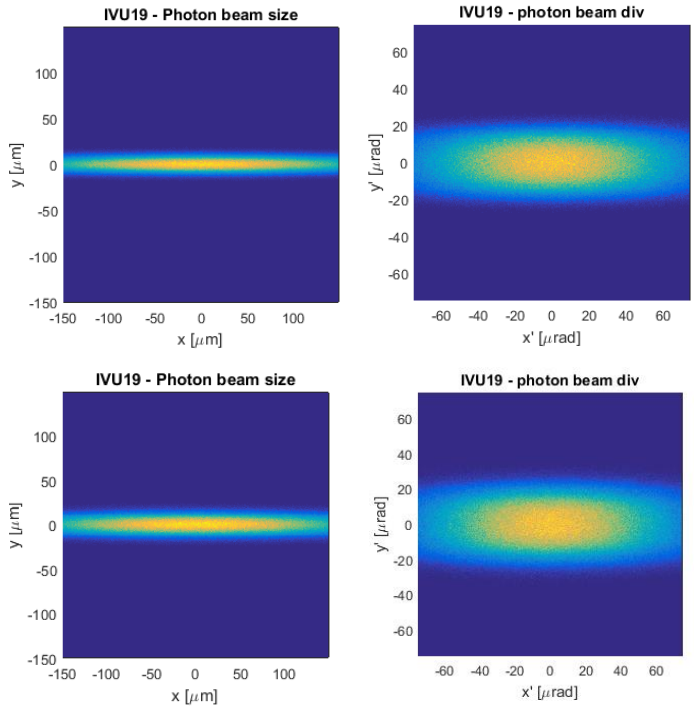

Figure 2. Source size and divergence as modelled by ART raytracing program at 12.661 keV (*top)* and 4 keV (*bottom*).

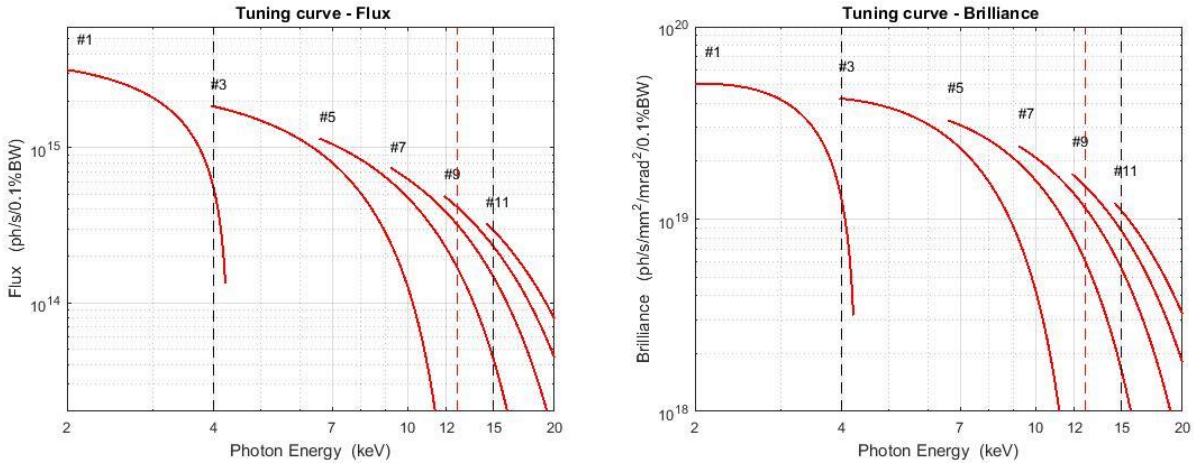

Figure 3. Tuning curves for integrated flux (left) and brilliance (right) at 250 mA in the storage ring. Minimum assumed magnetic gap is 5.2mm, which corresponds to K=2.14. Useful energy range of the beamline is marked in black dashed lines. The 3rd harmonic falls at 4 keV (lowest photon energy). Beam at a photon energy of 12.661 keV (dashed line in red) is achieved by the 9th harmonic.

2.3 Power

Given the magnetic length and the deflection parameter K of the IVU19, the total power is very high, reaching ~4 kW at 250 mA (nominal current) and ~7 kW at 400 mA (maximum current) circulating at the storage ring. The source angular power distribution is shown in Figure 4. In view of the high power load produced, the management of the power will follow strategies typically followed by wiggler beamlines, based on limiting the accepted aperture using masks and sharing the power budget between several elements.

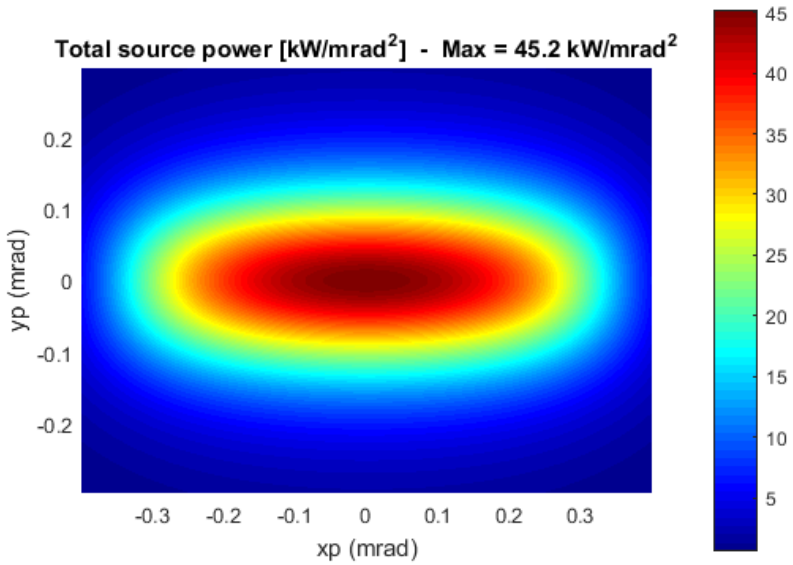

Figure 4. Angular power distribution of the IVU19 at a current of 400 mA in the storage ring.

3 Front End

The front end proposed for XAIRA is the standard front-end lay-out for undulator beamlines developed at ALBA and used in all the previous beamlines with similar sources (Figure 6). The design of the front end is based in:

- Two sets of masks, a fixed mask upstream, and a moveable mask downstream
- A single XBPM used to monitor the changes in the direction of the beam
- A photon shutter and a double bremsstrahlung shutter
- A trigger unit placed at the optical hutch, which allows the anticipated closure of a fast valve

The requirements on the apertures of the masks are critical, as the photon source delivers a power up to 7 kW. As in the case for wiggler beamlines, the limitation of the masks aperture is mandatory to establish a maximum power to be absorbed by the critical optical elements.

The fixed masks have an angular aperture of 0.35×0.267 mrad^2. This aperture allows a maximum transmitted power of 3013 W at 400 mA. This amount of power can not be handled by the beamline optics, and it has therefore to be further reduced by the following optical element of the front end, that is, the moveable masks.

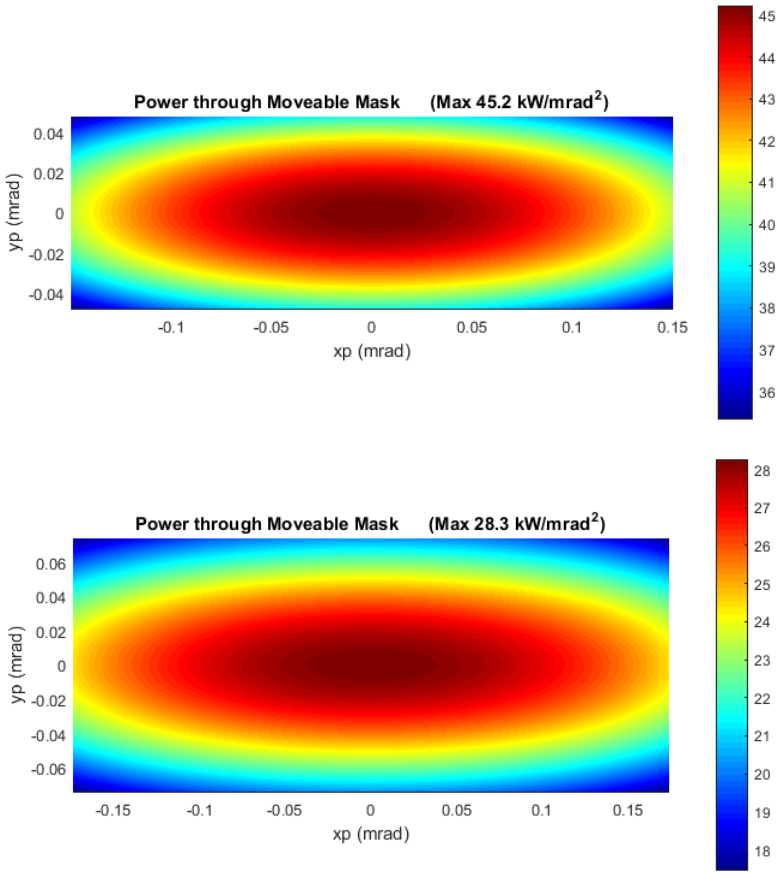

Figure 5. Flux density distribution through the fixed masks in worst conditions (400 mA in storage ring, top) and through the moveable masks when fully open in working conditions (250 mA in storage ring, bottom). In both cases the total flux through the slits is ~1300W. This is to be compared with the opening of the central cone (2 FWHM ~ 0.2×0.06 mrad^2).

It is foreseen two maximum allowed gaps of the moveable masks (Figure 5). Up to 250 mA the maximum allowed angular aperture is 0.35×0.15 mrad^2. At that current in the storage ring the power passing through the moveable masks is 1289 W. Above this current, the maximum angular aperture allowed for the moveable masks will be 0.3×0.1 mrad^2 to reduce the power arriving to the downstream optical elements. The power going through the moveable masks at this reduced aperture and a current of 400 mA is 1301 W (814 W if the current was 250 mA).

Therefore, the maximum power arriving at the optical elements of the beamline will be at most 1300 W, both at working (250mA) or worst (400mA) conditions. According to the design of the FE, the fixed mask will be placed at 10.94 from source, whereas the moveable masks will be placed 12.8-13.3 m (Figure 6). The functional layout of the front end is shown in Figure 7.

The specified angular apertures of the front end are much larger that the central cone of a tuned monochromatic beam (2 FWHM ~ 0.2×0.06 mrad^2) and, therefore, do not impose any restriction on the operation of the beamline.

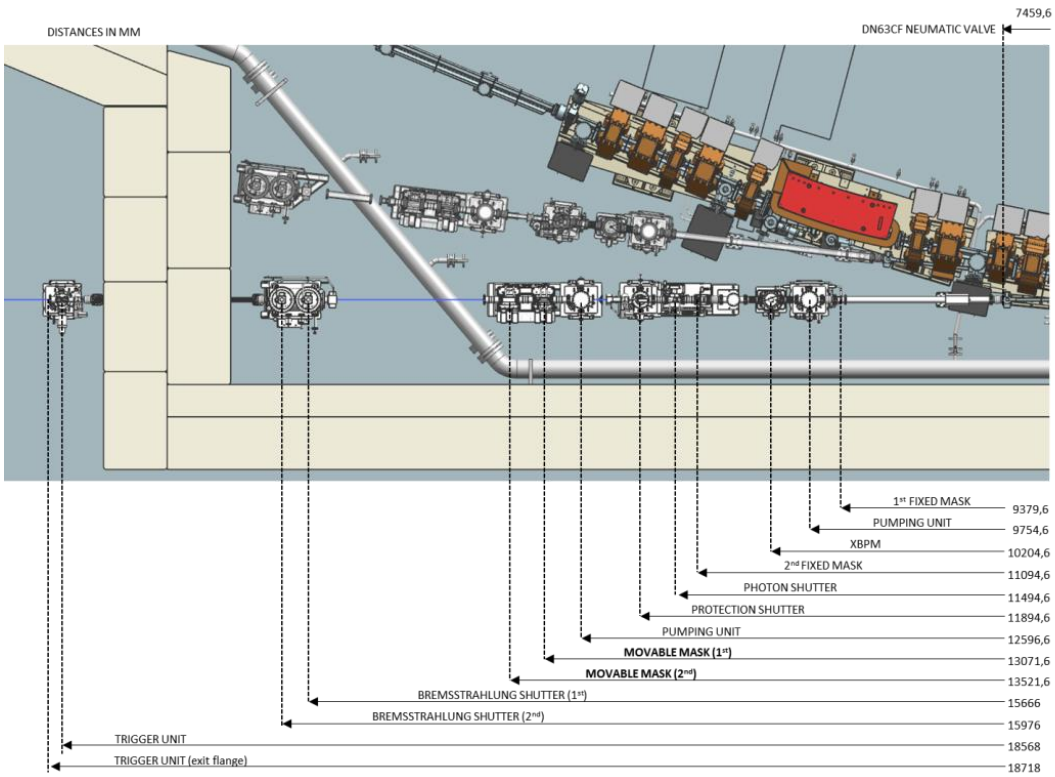

Figure 6. Lay out of the Front End installed at port FE06 as in the FE Conceptual Design Report

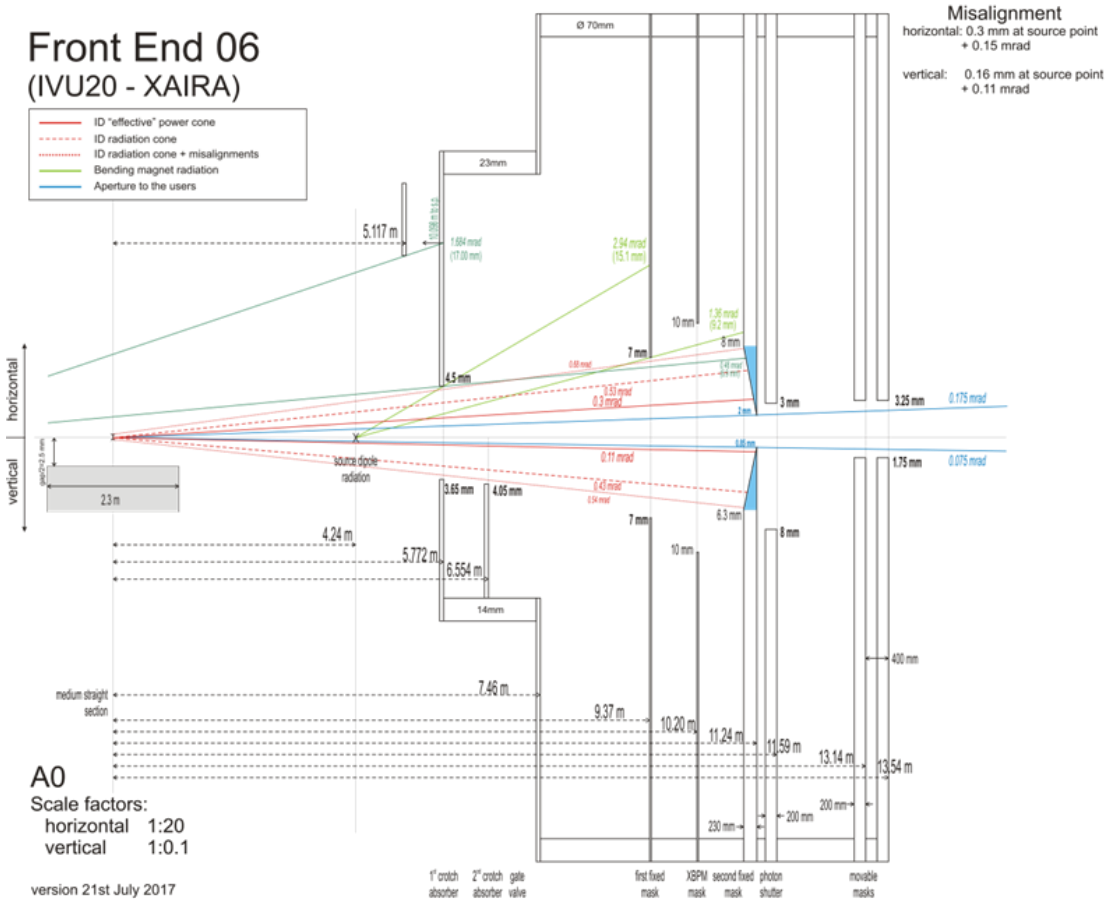

Figure 7. Functional layout of the Front End installed at port FE06 as in the FE Conceptual Design Report

4 Beamline optics

As defined in the design goals, the BL06-XAIRA beamline optics must provide an X-ray beam tuneable in the energy range of 4-14 keV and focused at the sample position to a size of ~3×1 μm FWHM. The focused beam needs to be stable and easy to align and change in energy and position.

The energy bandpass should be narrow enough to enable performing wavelength-dependent experiments. However, it would be desirable to have a high flux mode that takes advantage from the high frame rate of the state-of-the-art PAD detectors. This might be done at the expense of enlarging the bandpass of the monochromator by using a multilayer instead of a Si crystal.

The current optical lay out is based on meridionally-bent mechanical mirrors as a focusing optics, and a channel-cut monochromator, as sketched in Figure 1. The main characteristics of the optical elements are listed in Table 2. It includes a 2-stage horizontally focusing mirrors that produce a secondary source in horizontal direction which is adjusted by a pair of slits, a monochromator and a vertically focusing mirror.

Note that vacuum windows can not be used in the white beam, the reason being that the thickness of the window, either made of Diamond or Be, required to have an significant flux at

the low end of energy range (4 keV) does not allow this optical element to cope with the high power load from the undulator. As an example, a 300-μm thick Be window, which reduces the flux to the half at 4 keV, would absorb ~140 W at 250 mA circulating at the storage ring and the front end masks closed to 0.3×0.1 mrad.

It is also worth noting that in the process of designing the beamline it was proved by thermal FEA that a cryocooled Si monochromator could not withstand the high power and the high power density from the IVU19 undulator. Therefore, the horizontal prefocusing mirrors (HPM), with a much lower grazing incidence angle is required to be placed upstream the monochromator.

5 Monochromator

The proposed monochromator for XAIRA is the most innovative piece of instrumentation of the optical design. It foresees to combine a standard crystal monochromator together with a multilayer monochromator in the same crystal block. The two types of monochromator are presented separately, and the combined design is introduced afterwards.

5.1 Crystal monochromator

The design of the monochromator has to comply with the two main functions required to that piece of equipment, namely, the selection of the photon wavelength (energy) range to be used for the experiment and the dissipation of the power associated to the unselected wavelengths.

The most common method to select the photon energy in MX beamlines is the use of the diffracted X-ray beam from (111) reflection by silicon crystals. According to Bragg's law, the photon wavelength λ with a bandwidth Δλ is selected by adjusting the Bragg's angle θ of the crystals with respect to the incoming beam,

$$\lambda = 2d \sin\theta \qquad (2)$$

$$\Delta\lambda = 2d \cot\theta \, \Delta\theta$$

$$\frac{\Delta\lambda}{\lambda} = \cot\theta \;\; \Delta\theta \qquad (3)$$

where d is the plane spacing of the employed crystal reflection and $\Delta\theta$ is the divergence of the beam convoluted by the Darwin width, that is, the angular bandwidth in which a monochromatic beam is diffracted by the crystal planes.

Two main types of crystal mounting are usually chosen for MX beamlines according to the design priorities of the beamline. The most popular type of monochromator is the double-crystal monochromator (DCM), in which the second crystal surface is adjusted to maintain a fixed beam path after the monochromator at any photon wavelength. Alternatively, the channel-cut monochromator (CCM) mount, in which the two crystal surfaces are figured on the same silicon block, can be used. The CCM geometry improves radically the stability and the simplicity of the monochromator, which makes it less prone to introduce beam vibrations and drifts, at the expense of reducing the operation flexibility [3]. The output beam path of CCM employing in symmetric reflections (in which the silicon crystal is cut in a way that the crystal surface is parallel to the Bragg plane) varies according to

$$h = 2g \cos\theta \qquad (4)$$

where h is the beam excursion in the direction of the bounce and g is the gap between crystal surfaces. The case for g = 4.5 mm is shown in Figure 9 *left*. A Bartels monochromator, in which two identical DCMs or CCMs are placed oppositely, can be used to maintain the beam path after the monochromator at any selected wavelength. However, this option is disregarded for cost and operative reasons.

For long microfocus beamlines, the required high stability of the monochromator crystals can indicate a design with a vertical rotation axis, which minimizes the projection of gravity onto the Bragg axis and greatly reduces the construction's height above the supporting granite structure [13]. However, this choice sacrifices some flux at long wavelengths and energy resolution due to the polarization of the incoming photon beam. The vertical Bragg axis is therefore disregarded in the design, except in the event that future eventual vibrational FEA studies showed that the stability would be further improved.

In view of the characteristics of the different options, XAIRA will be equipped with a cryocooled CCM monochromator based upon Si(111) reflections. The reflections will be symmetric for ease of manufacturing and to preserve both beam size and divergence when changing the photon energy. The energy resolution $\Delta E/E$ is within 1.2-2×10^{-4} in the whole energy range (Figure 8). The choice is backed by the need to optimize the spatial stability of the beam, and by an easy beamline operation compatible with the dependence of the beam height upon energy.

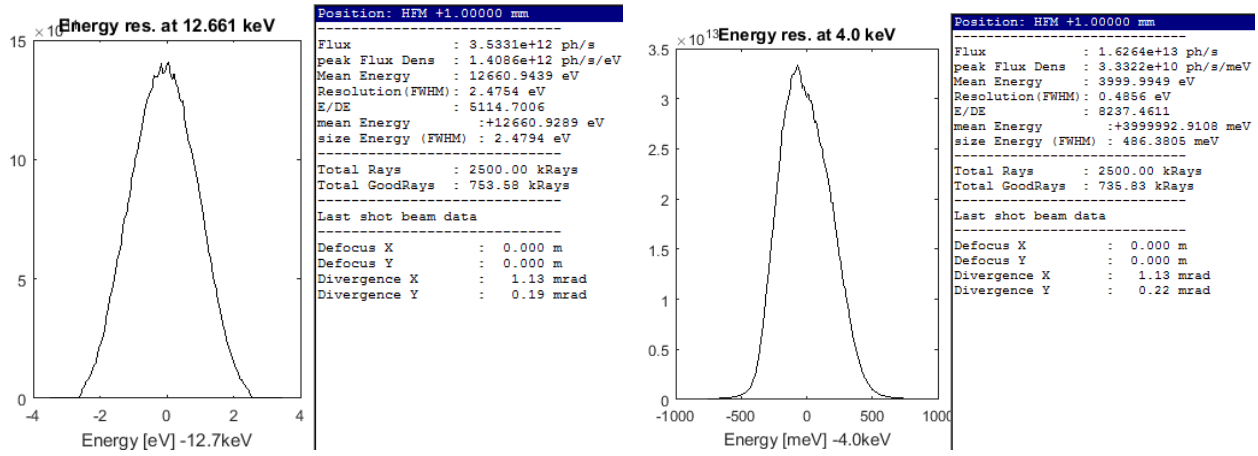

Figure 8. Beam Energy resolution at 12.661 keV (*left*) and at 4 keV (*right*) at the sample position.

The choice of a CCM is particularly convenient in microfocus beamlines as the beam dependence on the photon energy is reduced by the demagnification factor at the sample position if the focusing optics in the dispersive (vertical) direction is not adjusted and the optical axis preserved. Moreover, in order to further reduce the vertical beam excursion upon energy, the gap between the crystals will be as small as allowed by safety considerations, that is, 4.5 mm. The high demagnification ratio and the low gap result in a beam excursion at the sample position of only 60 μm in the whole 4-14 keV energy range (Figure 9). This reduced beam excursion at the sample position makes the CCM (or similarly a pseudo channel cut) not a fixed *exit beam* monochromator, but an effective fixed *sample beam* monochromator.

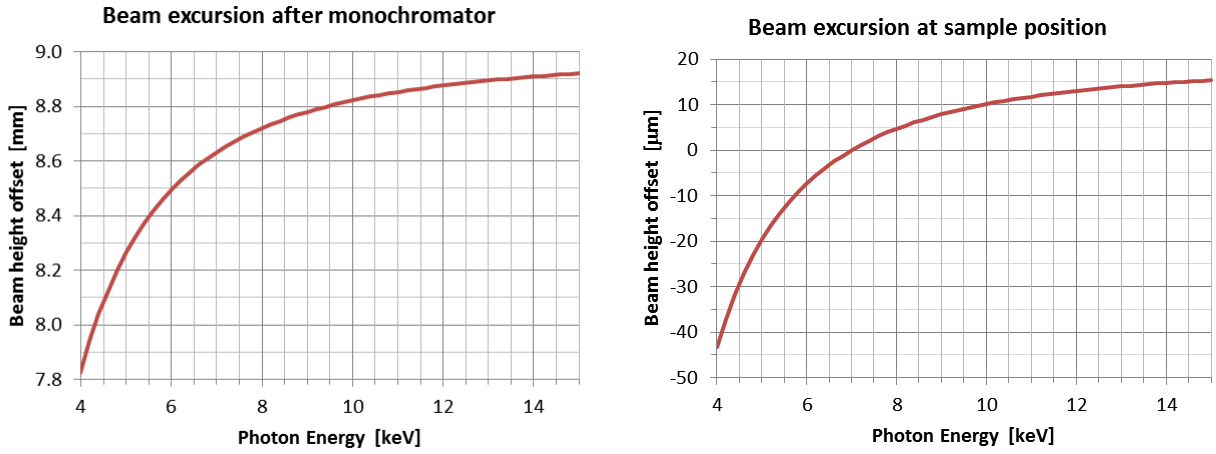

Figure 9. Beam excursion of channel cut monochromator with a gap between surfaces of g = 4.5mm. (*left*) Beam excursion after the monochromator, following eq. 4. (*right*) Beam excursion at the sample position after the source demagnification provided by the VFM. The latter curve assumes that the position of the VFM is not adjusted upon energy and therefore the beam footprint travels along the mirror surface upon energy.

5.2 Multilayer monochromators

Monochromators based on diffraction by multilayers instead of silicon crystals produce a wide energy bandpass, and hence large photon flux throughput. Multilayers as elements selecting the energy were first used in MX experiments 20 years ago [14], although only recently, with the advent of the low *d*-spacing multilayers, the use has been spread for routine use to exploit the newly available high frame rate detectors and new fast data collection strategies. Current MX beamlines using water-cooled multilayers are VMX-µ at Diamond [15] or BioCAT at the APS [16]. Water cooling is usually employed in multilayer monochromators and mirrors due to the low grazing incidence angles. However, cryogenic cooling can also be employed safely without damaging the periodic structure [17].

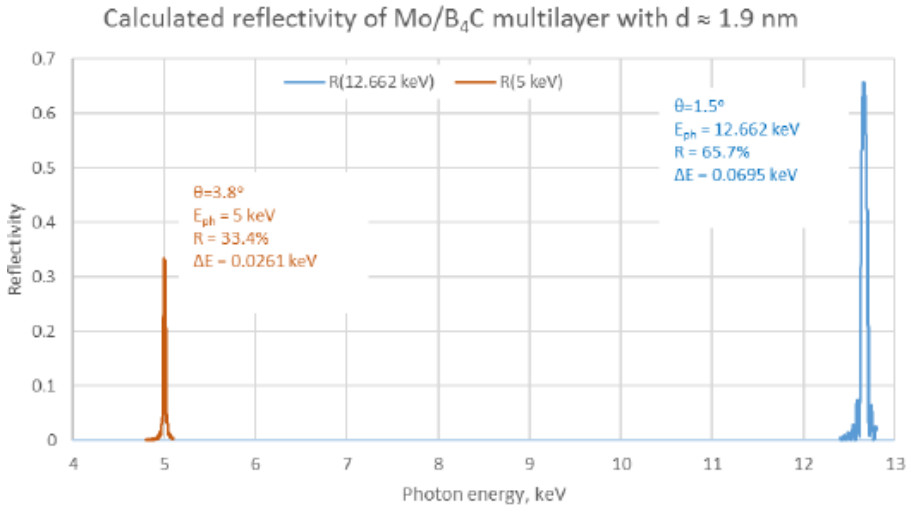

Figure 10. Calculated reflectivity of Mo/B_4C multilayer structure with d-spacing of ~1.9 nm by Rigaku. Imperfections of the multilayer such as interfacial roughness were taken into account. Imperfections of the substrate were not taken into account.

Low *d*-spacing multilayers are required to keep a high grazing angle. Currently a good multilayer is the Mo/B_4C with a d-spacing of ~1.9nm, as used in the SAXS/WAXS beamlines BL23A at the NSRRC and 7.3.3 at the ALS. Other possible choices are Ru/B_4C [18] and Th/B_4C. The corresponding Bragg axis according to eq. 2 is around 1.5 degrees at ~12 keV. All these structures are commercially available (Figure 10).

The output flux using a multilayer can be one order of magnitude higher than the flux obtained by the standard Si(111) reflection, at the expense of reducing the monochromaticity of the X-ray beam. While the energy resolution from the Si(111) reflection is $\Delta E/E$ is ~2 10^{-4} (0.02%), the resolution obtained in a typical multilayer ranges between 0.5% and 2%. This energy resolution is too low for wavelength-dependent MX experiments performed at the absorption edges. Nevertheless, the energy resolution obtained with the multilayers above is suitable for wavelength-independent experiments, or eventually for SAD experiments exploiting the anomalous signal far from the absorption edges, where the change of the anomalous contribution of the structure factor is negligible in the energy range selected by the multilayer.

The output flux F through a multilayer or a crystal monochromator is proportional to the integrated reflectivity of the diffracting element, that is, the area under the rocking curve,

$$F(E) \propto \int_{E_{min}}^{E_{max}} R_c(E)dE \qquad (5)$$

The integrated intensity of multilayers is typically much larger than that produced by crystals, and in particular Si(111), due to the much larger Darwin width, which largely compensates the loss of flux due to the lower reflectivity of the multilayer. However, the roughness of the substrate and the interfaces between layers play an important role in the final output flux of the multilayer. Calculations using IMD software [19] show that above a few angstroms RMS roughness the integrated intensity drops dramatically (Figure 11). Interfacial roughness and number of bilayers also play an important role in the final integrated intensity.

Taking into account all these factors, typical flux gains are in the range of one order of magnitude with respect to Si(111) crystals (Table 6).

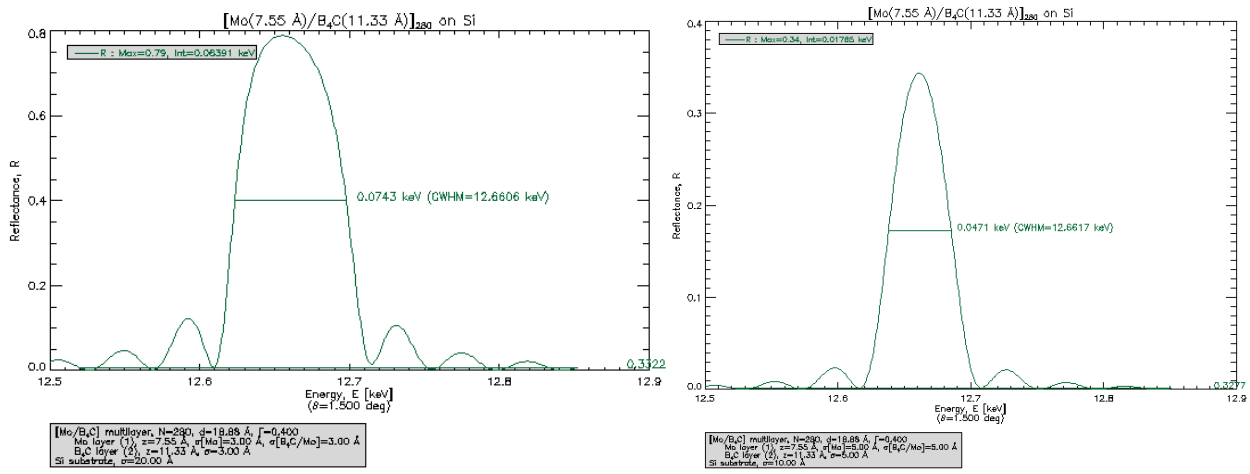

Figure 11. Reflectivity of a Mo/B_4C multilayer assuming a RMS roughness of 3 Å (*left*) and 5 Å (*right*) of the substrate.

Diffracting structure	Integrated intensity at 12.661 keV	Gain factor
Si(111)	0.02%	1
Mo/B_4C (3 Å RMS roughness)	0.50%	≤25
Mo/B_4C (5 Å RMS roughness)	0.13%	≤7

Table 6. Integrated intensities at 12.661 keV of Si(111) and Mo/B_4C at 2 different roughness, calculated using IMD program (Figure 11) and equation (5). The multilayer parameters are listed in Table 7.

5.3 The CCM/DMM concept

The relatively large grazing incidence angle of the multilayers in the hard X-ray range opens up the possibility of depositing them on Si channel cut monochromators, which have dimensions limited by the diameter of the Si crystal rod. This is the basis for the Channel Cut Mono/Double Multilayer Mono (CCM/DMM) that is proposed for XAIRA. CCM/DMM is a novel design in which a multilayer is grown at the ends of the optical surfaces of a channel-cut crystal (Figure 12). The Bragg axis is placed at a distance l underneath the first optical surface, and intersects the beam axis. In this configuration, the center of the beam travels along the crystal surface to a position Δy according to

$$\Delta y = \frac{l}{\tan\theta} \qquad (6)$$

where l is positive when the Bragg axis is underneath the crystal surface and Δy is positive in the upstream direction, i.e. towards the end of the crystal away from the second crystal. Being l a fixed parameter of the design, the position of the beam depends solely from the Bragg angle θ. Assuming a distance of l=2.5 mm and an energy range of 4-14 keV, the beam travels by ~14.4mm for Si(111) and by ~86.6 mm for any multilayer with a d spacing of 1.95 nm (Figure 13). Most importantly, the ranges of beam positions for both diffracting means do not overlap, making this design feasible from the geometrical point of view, as the multilayer must be grown on an area of the crystal that is not required to be used by the Si(111).

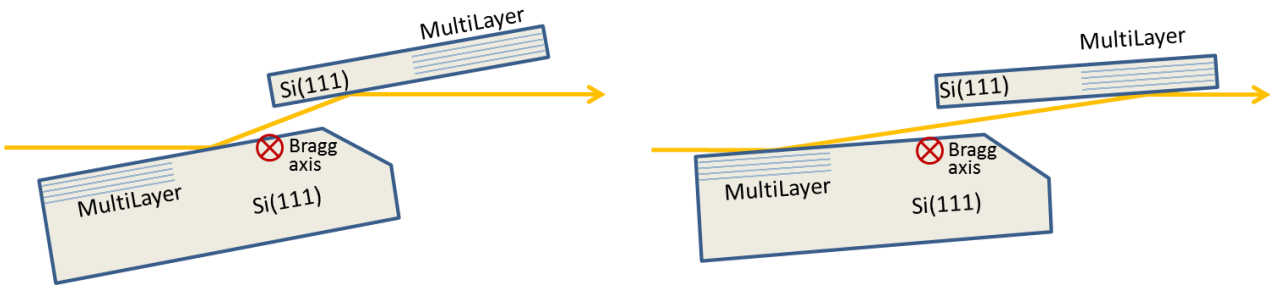

Figure 12. Concept of the CCM/DMM design, combining a Si crystal and a multilayer in a channel-cut mounting. (*left*) the beam is diffracted by the Si(111) reflection of the crystal. (*right*) the beam is diffracted by the multilayer. The Bragg angle lies 2.5 mm underneath the surface of the first crystal, so that the beam travels along the surface depending on the Bragg incidence angle and according to eq. (6).

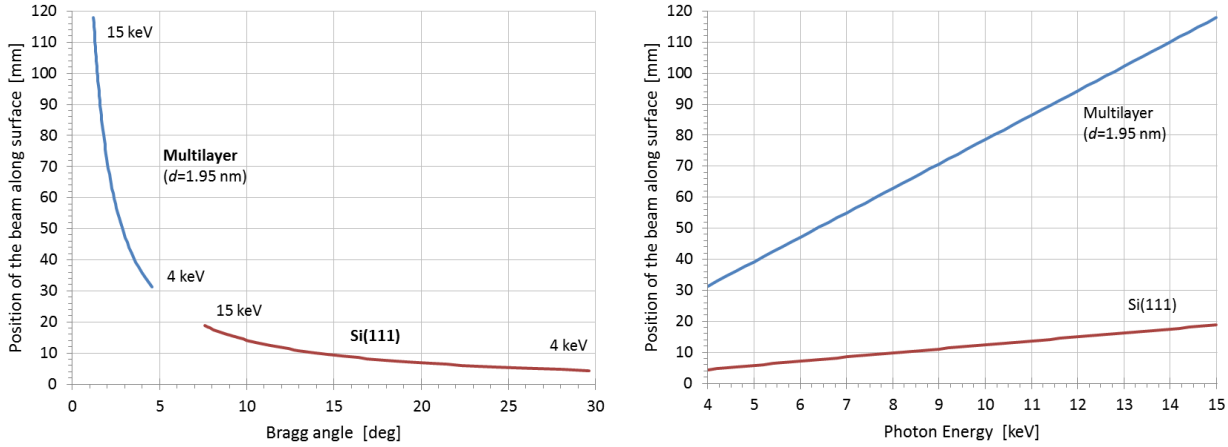

Figure 13. (*left*) Dependence of the position of the beam along the first crystal surface for the Si(111) reflection and a multilayer with a *d* spacing of 19.5 nm on the Bragg axis, following eq. (2). (*right*) Dependence of the position of the beam on the selected energy for the same diffracting structures. The Bragg axis is 2.5 mm underneath the first crystal surface (Figure 12), and is assumed to be coplanar with the input X-ray beam

A relevant issue of this design is the polishing quality of the crystal surfaces on channel cut monochromators. Current technology typically allows polishing the surfaces of the channel-cut crystals down to a RMS roughness of 10 Å, but it might be possible to optimize up to 3 Å. The reduction of the output flux of the multilayer due to a poor polishing quality of the substrate can be avoided by using a pseudo channel cut design, in which two separate, optimally polished flat crystal surfaces are clamped together to simulate a channel cut configuration.

5.4 Design of the CCM/DMM monochromator

The proposed final design for the XAIRA is a combined CCM/DMM monochromator as designed in section 5.3. We impose the geometrical dimensions of the channel cut block to be compatible with a standard 12" Si crystal rod. This added constraint reduces the available energy range of the multilayer to 4-12.6 keV (see Figure 13) and leads to the optimum geometry shown in Figure 14. The monochromator is cryocooled using LN_2 through copper external heat exchangers placed in both sides of the first crystal block.

The silicon optical surfaces are oriented following the crystal face {111} symmetrically cut. The gap between optical surfaces is 4.5 mm. On a limited area given by Figure 14, the multilayer is to be grown according to specifications listed in Table 7. The current instrumentation and multilayer growth procedures allow growing the multilayer on a channel cut monochromator provided that the substrate surface is not facing the second optical surface, and has a buffer distance of several cm in which the crystal block is not protruding the surface where the multilayer has to be grown.

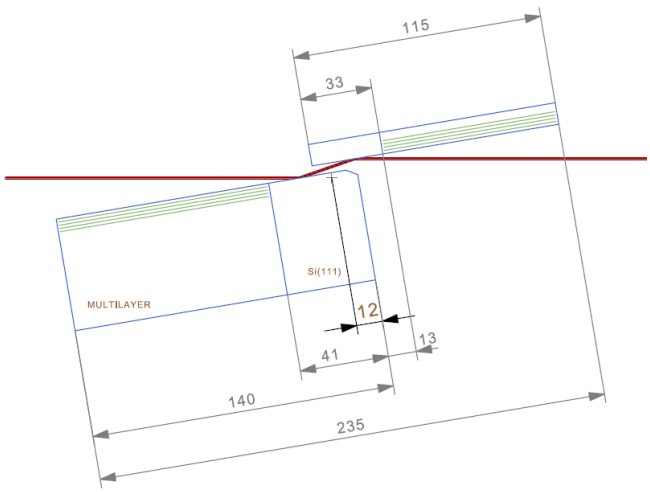

Figure 14. Dimensions of the dual Si(111)-Multilayer channel cut design proposed for XAIRA.

Parameter		Value	Comments
Bilayer components		Ru/B_4C	Other possible candidates: Rh/ Ru/B_4C, Mo/B_4C
Period [nm]	2d	1.9-2.0	The lowest possible, without increasing the interface width
Number of bilayers	N	280	
Bilayer ratio	Γ	0.4	
Energy bandpass	ΔE/E	<1%	
Interface width		<3 Å	
Substrate roughness		<3 Å	Critical parameter to minimize. Current standard value in channel cut mono is 10 Å

Table 7. Specifications of the multilayer.

The advantages of the CCM/DMM design are the following:

1. Allows two different monochromators with the same mechanical complexity.
2. Compact design
3. Minimizes the effects of vibrations and drifts as both crystal surfaces are mechanically and thermically linked.
4. No need for extra motors or adjustments required for the multilayer
5. Easy exchange of diffracting surfaces, only by rotating the Bragg axis. This is relevant in MX experiments, where several projects are included in each beamtime.
6. Easy mechanics, less prone to failures or leaks.
7. The narrow gap between surfaces allows a small vertical beam position change, which is further reduced by the vertical demagnification factor (see section 6.2).
8. Easier commissioning

Nevertheless, this design has three identified risks that need to be addressed:

R1. **The substrate roughness is not optimal to grow a multilayer**
The current standard roughness for channel cut surfaces is 10 Å, significantly poorer than that achieved in single flat surfaces (1 Å). A poor roughness is acceptable for crystal diffraction, but it is not for multilayer diffraction. Polishing can be improved to reduce the roughness down to 3 Å[1], but an engagement of the companies is required.

R2. **The optical surface does not have enough clear space above to be polished**
The polishing instruments have geometrical requirements to be used. Usually the optical surface to polish is required not to have protruding elements. This is accomplished for single optical surfaces such as in DCM or pseudo-channel cut monochromators (pCCM), but it is not for CCMs.

R3. **The multilayers of the two optical surfaces have different characteristics**
In a CCM, the two optical surfaces must be grown separately due to their opposite bounce orientation. Even though the surfaces are specified to be identical, the possible different substrate quality and the uncertainty in the multilayer growth process may produce differences that may result in different diffracting characteristics.

These risks need to be carefully evaluated with the substrate and the multilayer manufacturing companies. Several actions can be implemented to avoid or mitigate the effect of these risks:

A1. **Change the polishing method of the substrate.**
Several methods can be used to polish the crystal surface after the chemical etching, including planetary systems, linear movements and hand polishing. A careful selection of the polishing method is required to adapt to the geometry of the channel-cut crystal.
This action may mitigate R1 and R2 risks

A2. **Reduce the area in which the multilayer is grown. Reduce the covered energy range.**
The length of the area in which the multilayer is to be grown is 99 mm and 82 mm for the first and the second optical surfaces, respectively (Figure 14). This allows the multilayer covering the energy range 5-12.6 keV. However, the area can be reduced to ~55 mm and ~50 mm if we reduce the energy range to cover to 10-12.6 keV (as derived from Figure 13, *right*). In this case, the multilayer should be grown only on the most external region of the optical surfaces, easing the polishing process.
This action may mitigate R1 and R2 risks.

A3. **Increase the multilayer period to reduce the effect of the substrate roughness.**
The roughness of the substrate plays is increasingly affecting the output flux as the *d*-spacing of the multilayer is decreasing. In case the roughness is severely limiting the flux gain, a multilayer with a larger period may be envisaged at the expense of decreasing the Bragg angle. A shallower Bragg angle reduces the energy range in the high-end limit or, alternatively, compels to manufacture crystals with longer optical surfaces.
This action may mitigate R1 risk.

[1] Personal communication.

A4. **Choice of the multilayer characteristics (material, bilayer ratio) to reduce the effect of the reproducibility in the growing process.**
Usually the material characteristics, notably the material and the bilayer ratio Γ, are selected to maximize the flux and maximize the Bragg angle. Nevertheless, other objectives can be used to select the multilayer characteristics:
- Choose the multilayer material to ensure a higher reproducibility in the growing process.
- Increase the energy bandpass to reduce the dependence of the reproducibility in the growing process.

This action may mitigate R3 risk.

A5. **Replace the channel-cut block by a pseudo-channel-cut mount**
An alternative to the CCM design is to implement a pseudo-channel-cut monochromator (pCCM), as implemented in ID01 at the ESRF or in 8-ID-I at the APS [20]. This design is based on two crystal surfaces polished separately, and later clamped together to simulate a channel cut.
This action mitigates R1, R2 and R3 risks. However, the pCCM increases significantly the complexity of the device. Besides, the correct alignment of the surfaces is critical, and may affect the performance of the Si(111) reflection.

Other risks and actions may arise in the manufacturing process. Nevertheless, all the risks associated with the CCM/DMM design affect exclusively the multilayer performance. The Si(111) reflection is not affected either by these risks nor by the actions to mitigate the risks, except for the implementation of a pCCM (action A5). In the worst scenario in which the multilayer is proven to be ineffective to produce a significant gain in flux, the CCM/DMM design may always be used as a CCM design. The center of the beam would only be traveling along the first crystal surface by 15mm in the whole 4-14 keV energy range.

6 Focusing optics

The focusing optics is based on plane-elliptical reflecting mirrors, whose basic parameters are listed in Table 2. The characteristics of the photon source (Table 3) and the performance requirements lead to a minimal focusing optics design based in two stages in the horizontal direction, and one stage in the vertical direction. The choice of a channel-cut monochromator, which moves vertically the beam upon changes in energy, encourages the option of using a single focusing stage in the vertical direction instead of two stages to ease the beamline operation. Furthermore, the use of non-dispersive reflecting mirrors allows the operation of the beamline independently of the photon energy.

The final positions and lengths of the mirrors (Table 2) have been studied thoroughly, exploring all the possibilities left by the following geometrical constraints:

- Minimum distance between the HPM and the HSS to place the monochromator (q_{h1}>2 m)
- Minimum distance between optical surfaces of the VFM and the HFM (>145 mm)
- Minimum working distance between the end of the last mirror and the sample position (d_w>0.6 m)

Other imposed constraints are the required beam size at the sample position and a limit of a minimum of 40% of the collected flux with respect to the total. The total length of the beamline and the distance between the HPM and the HSS (q_{h1}) are effectively the only parameters subject to variation (Figure 15). Some figures of merit that included the flux, the focal beam spot area and dimensions and the total length of the beamline (for cost reasons) were calculated (Figure 16).

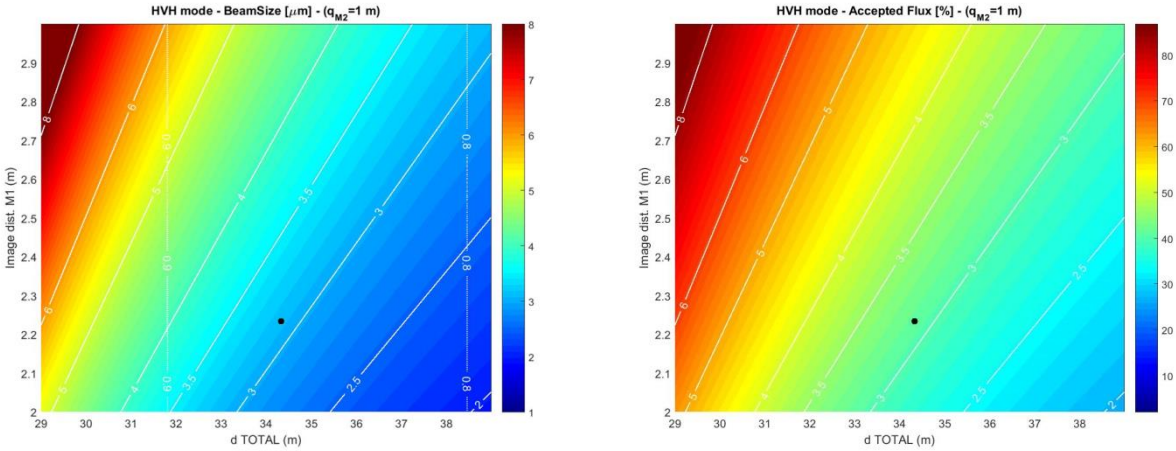

Figure 15. Explored space of positions of the horizontal focusing optics. The contour white lines and the thinner, vertical lines mark the horizontal and the vertical beam size at the sample position, respectively. The black point corresponds to the final parameters of the beamline. The geometrical constraints not shown in this plot play an important role in defining the final position.

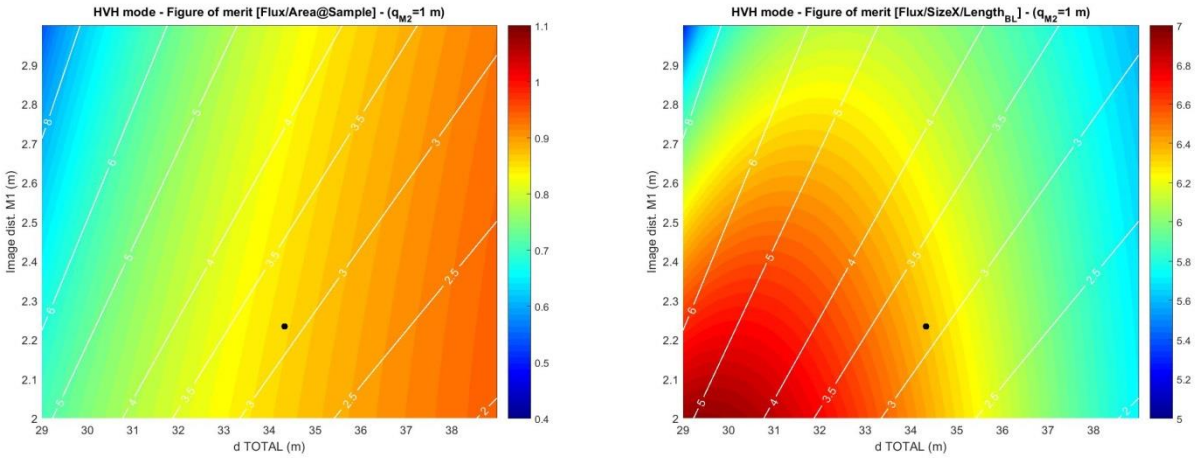

Figure 16. Considered figures of merit to converge to optical focusing optics. The black point corresponds to the parameters of the beamline. Contour white lines mark the horizontal beam size at the sample position. The geometrical constraints not shown in this plot play an important role in defining the final position.

6.1 Beam characteristics at the sample position

The final parameters of the beam at the sample position are listed in Table 8. These are compatible with the beamline requirements as shown in Table 1. The beam size was calculated analytically (Figure 17) and by raytracing modelling (Figure 18) using ART suite are in good agreement and are essentially independent of the photon energy.

The flux of the beamline remains over $3 \cdot 10^{12}$ ph/s in the useful energy range. Highest flux is achieved at the low energy limit (4 keV) with the harmonic #3 and decreases monotonically with energy. The values from the analytical calculation for the whole energy range (Figure 19) are systematically a factor ~2 higher than those modelled by raytracing (Figure 18).

Beam size at 12.661 keV (FWHM, h×v)			μm	3.1×0.8
Beam divergence at 12.661 keV (FWHM, h×v)			mrad	2.6-3 × ~0.6
Accepted flux fraction by mirrors in hor. direction				41.2%
Accepted flux fraction by mirrors in vert. direction				100%
Total flux at sample at 12.661@250 mA			ph/s	$3.5 \cdot 10^{12}$
Total flux at sample, whole energy range @250 mA			ph/s	$3\text{-}20 \cdot 10^{12}$
Energy resolution	Si (111)	(4-14 keV)		$1.2\text{-}2\ 10^{-4}$
	Multilayer	(4-12.6 keV)		TBD

Table 8. Beam characteristics at the sample position.

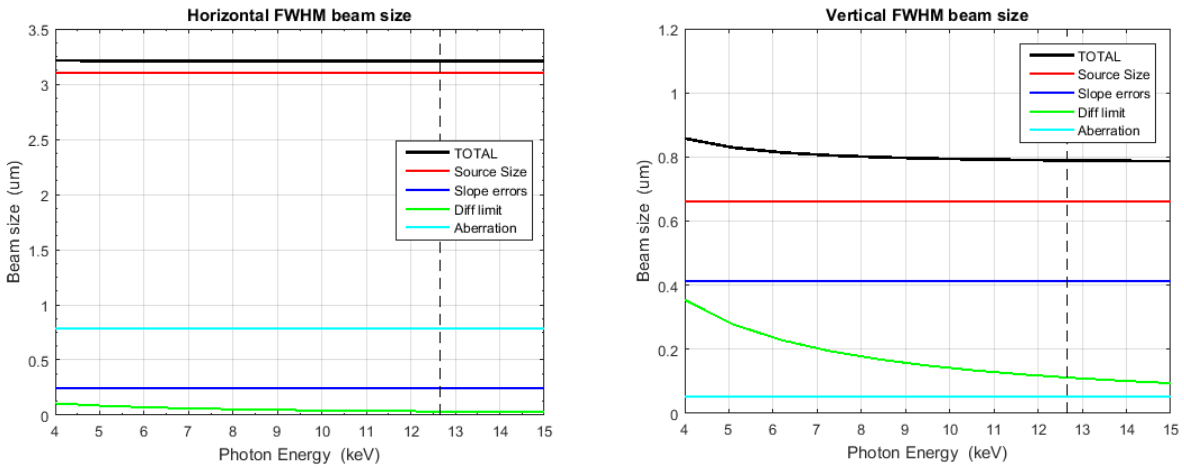

Figure 17. Analytical calculation of the beam size and divergence for the horizontal (*left*) and vertical (*right*) dimensions. The source size is assuming only the electron beam size. Aberrations are assuming a contribution of 10% of the higher order spatial harmonics from the ideal polynomial torus that can not be compensated by the parabolic mirror figure produced by the motor actuators. Actuators installed along the optical surface, such those implemented in bimorph mirrors or the ALBA nanobender, may reduce that contribution to zero.

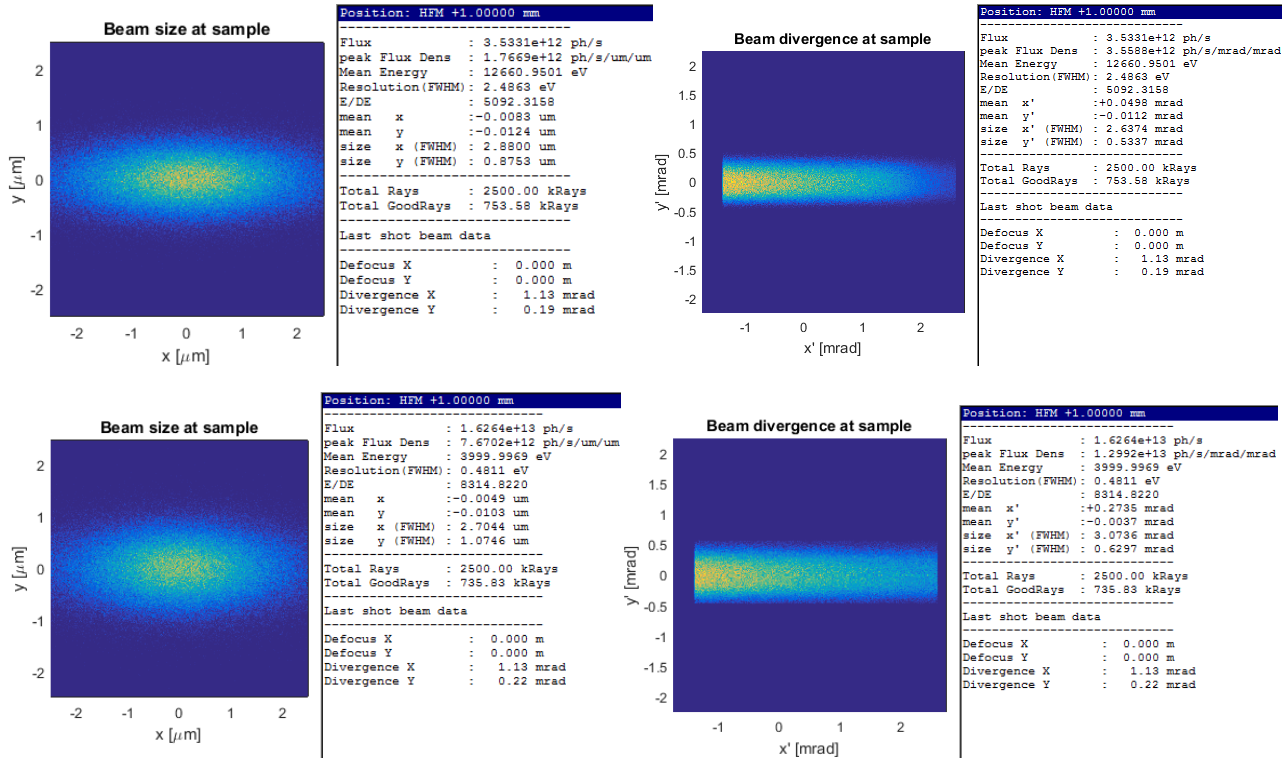

Figure 18. Nominal beam size and divergence at the sample position at 12.661 keV (*top)* and at 4 keV (*bottom*).

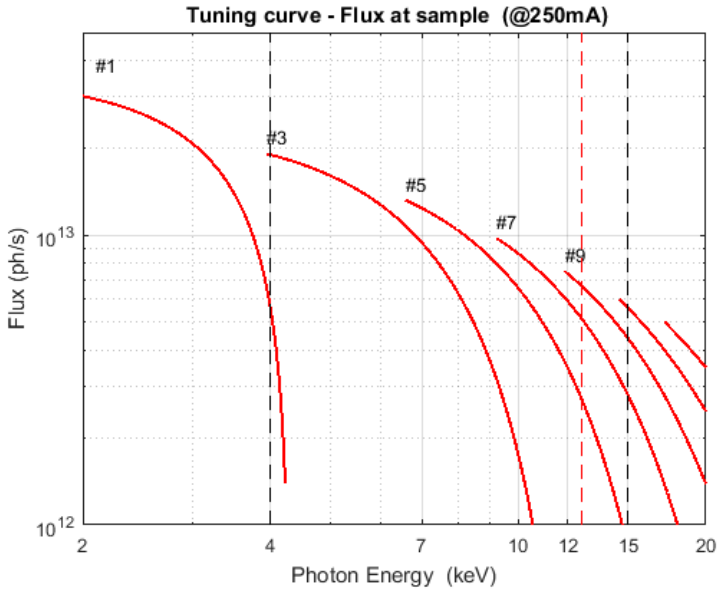

Figure 19. Flux at the sample position calculated analytically for Si(111). The plot is that of (Figure 3 *left*) but including the reflectivity of the mirrors and the channel-cut crystal, and a flux fraction accepted by the mirrors of 41%. The assumed energy bandwidth $\Delta E/E$ is linear, with values of $1.2 \cdot 10^{-4}$ at 4 keV and $2 \cdot 10^{-4}$ at 12.661 keV, as obtained by raytracing (Figure 8).

6.2 Adjustment of the focusing optics upon energy

It is important to discuss and evaluate the adjustments required on the beamline optics due to the variable exit beam height downstream the channel-cut monochromator. The monochromator, as specified for XAIRA, changes the beam height by ~1.1 mm over the whole energy range (Figure 9). In the horizontally focusing mirror this leads to a shift of the beam across the mirror surface (i.e. transversally to beam axis) by the same amount. Since the coating stripes of the mirror are much wider (typically 8-12 mm) and the effect of the sagittal slope errors is negligible, the HFM has not to be adjusted when changing the photon energy within the whole useful range of the beamline.

Special attention has to be paid to the effect of the variation of the beam height upon energy on vertical focusing mirror. The center of the beam will travel along the optical surface of the VFM by $\Delta h/\sin\theta$, where Δh is the change of the beam height according to (Eq. 4), and θ is the grazing incidence angle on the mirror. This leads to a total travel of the beam along the optical surface of 244 mm. The flux can be collected in the whole energy range following two strategies:

- Move the VFM to follow the beam. This method keeps the center of the beam at the center of the mirror for the whole energy range. The beam at the sample position changes its vertical position by the same amount than the beam offset produced by the channel cut monochromator (~1.1 mm for 4-14 keV).
- Let the beam travel along the mirror surface. The VFM is not adjusted in height, and the beam moves along the surface. The mirror should be long enough to cope with the total travel excursion within the energy range (244mm) plus the beam footprint on the mirror (≤240mm).

The optical design presented in this document foresees the second option, that is, to let the beam travel along the mirror surface, for two main reasons. First, the beamline optics simply does not need any adjustment upon a change in the photon energy, which greatly eases the operation, at the expense to increase the optical length of the mirror to 400-500 mm. Second, keeping the mirror fixed reduces the vertical movement of the beam at the sample position by the demagnification factor in the vertical dimension, D_v = 18.7. Using this strategy, the beam moves vertically by 58 μm in the entire 4-14 keV range, and only by 14 μm in the most commonly used 7-14 keV range.

Previous experience in beamline BL13-XALOC at Alba operating without moving the VFM has been very successful since the beginning of user operation in 2012 [21]. At this beamline the beam movement at the sample position is completely reproducible, and is automatically corrected by moving the sample table according to a look-up table to an accuracy of 1-3 μm. The beam can be further steered using a diagnostic at the sample position if required.

Moreover, the two strategies are not incompatible. The vertical movement of the VFM is motorized and consequently, the possibility of adjusting the height of the VFM if required at very low energies is not precluded by the foreseen strategy.

6.3 Mirror parameters

The geometry and characteristics of the mirrors and the benders can be calculated using the elastic beam theory [22]. We foresee to use rectangular or trapezoid mirror shapes, with flat surface (nominal radius of curvature infinite). We assume two independent actuators which can bend the optical surface to a parabolic figure. The bender actuators are assumed to produce a maximum force F_U and F_D of 1000 N.

Moreover, there have been several efforts to introduce further actuators to modify the optical surface and correct for the gravity sag and the long-wavelength slope errors. The most commonly used system are the bimorph mirrors, based on piezo elements [23], although other projects in several synchrotrons have been based on mechanical benders. In particular, the nanobender system [24], which has been developed at ALBA, has implemented a tailored figure correction at nanometric precision. According to this availability, we assume that the gravity sag and the long-wavelength figure errors of the mirror are corrected by a small number of actuators, limited by the length of the mirror, which can be adjusted in force and position.

The values of the parameters resulting from the mirror bending optimization are listed in Table 9, and the resulting mirror surface shapes and the residual figure error are plotted in Figure 20. All parameters are kept in safe values and are well within the capabilities of synchrotron mirror manufacturers.

It is worth to note that the thickness of the HPM has to be compatible with the side cooling system. The proposed thickness, 30 mm, is fully compatible with the geometry described in §7.

	HPM	**VFM**	**HFM**
Object distances (p)	20.1 m	32.591m	11 m
Image distances (q)	2.233 m	1.743 m	1 m
Demagnification factor	9	18.7	11
Shape	Rectangular	Rectangular	Trapezoidal
Length	450 mm	400 mm	800 mm
Mirror thickness/width	30/40 mm	25/30 mm	20/30 mm
Bulk/Stripes	Si / Rh	Si / Rh, Si	Si / Rh, Si
Cooling	Water 23C	-	-
Beam grazing incidence angle	4.5 mrad	4.5 mrad	4.5 mrad
Polishing radius of curvature	infinite	infinite	infinite
Average radius of curvature	890.3 m	685.9 m	384.8 m
Minimum radius of curvature	775.2 m	604.3 m	200.9 m
Bending forces (upstream/downstream)	454/602 N	238/335 N	439/507 N
Figure error (RMS)	8 nrad	7 nrad	32 nrad
Corrector actuators	$N = 3$	$N = 4$	$N = 4$

Table 9. Mirror parameters after optimization

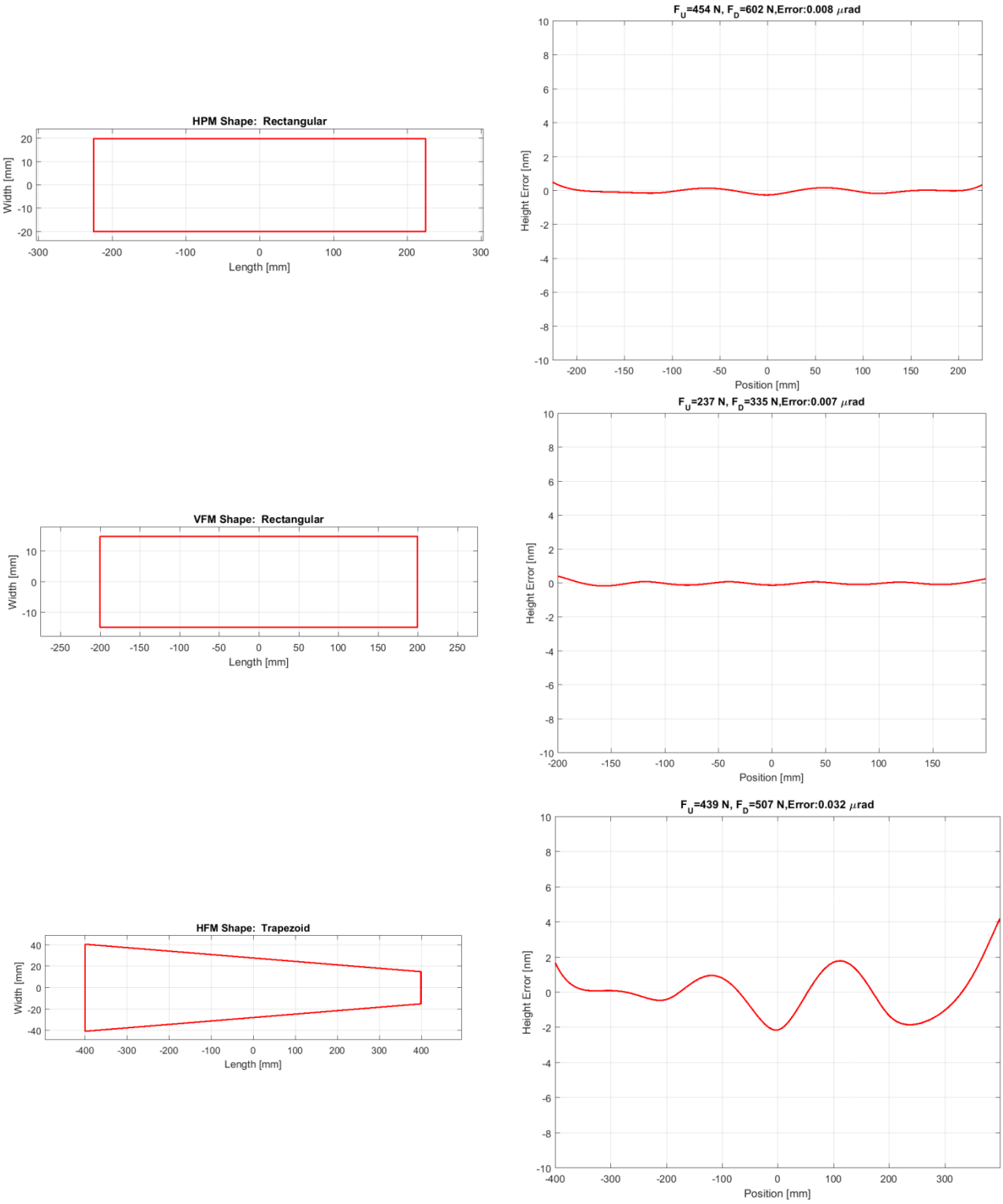

Figure 20. Mirror shapes and residual figure errors for the HPM (*top*), VFM (*middle*) and HFM (*bottom*) after removal of the best exact ellipse. The effect of the gravity sag is corrected for the VFM.

The grazing incidence angle of all mirrors is 4.5 mrad, and has been selected to produce a cut-off energy of 14 keV in the Rh stripe (Figure 21). The 3rd harmonic rejection is provided by the VFM and the HFM mirrors for the Si stripe, and by all the mirrors for the Rh stripe. The ratio of the 3rd harmonic rejection is kept well below 10^{-4} in the whole 4-14 keV energy range, which is further increased by the monotone reduction of photon flux with energy (Figure 3).

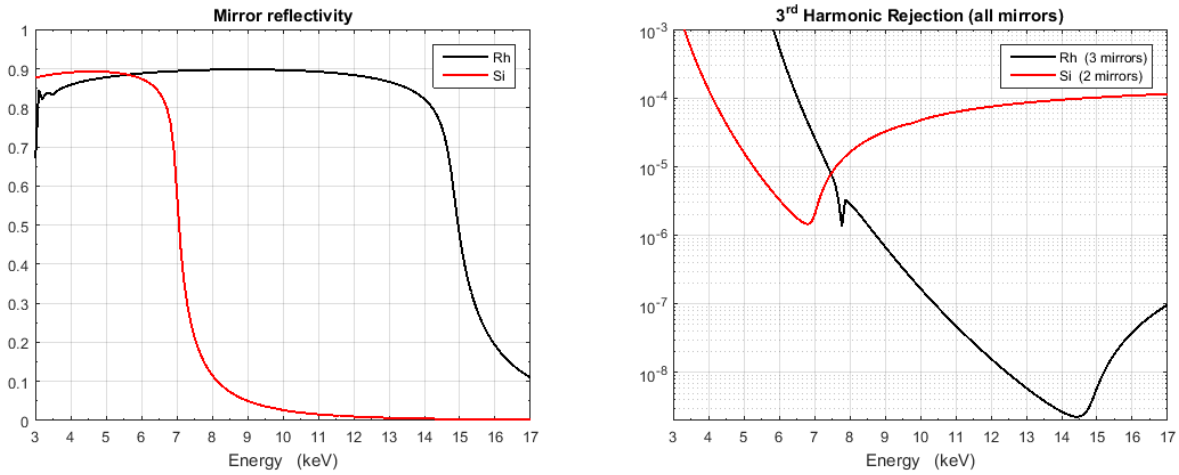

Figure 21. (*left*) Mirror reflectivity for the Si and the Rh stripes. (*right*) Ratio or the 3rd harmonic rejection provided by the VFM and the HFM mirrors combined. The dependence of the flux upon the photon energy and the energy bandwidth of the monochromator are not included, so real harmonic rejection factor may be better.

6.4 Footprints

Footprints of the optical elements are relatively constant within the useful energy range (Table 10). The footprint on the horizontally focusing mirrors (HPM, HFM) span along the whole optical surface, whereas the footprints of the optical elements with vertical bounce (X1, X2 and VFM) are shorter than the optical surface and travel along the surface upon the selected energy (Figure 22).

	HPM	**X1, X2**	**VFM**	**HFM**
Optical surface length	450		400	800
Beam travel 4-14 keV	0	13.3 (merid. dir.)	244 (merid. dir.)	<1 (sagittal dir)
Footprint length (FWHM) @12.661 keV, #9 harm	444	3.9 (9.064deg)	211	722
Footprint length (FWHM) @4 keV, #3 harm	444	1.5 (29.7 deg)	240	800
Footprint width (FWHM)	0.6	1.1	9.1	0.5

Table 10. Beam footprints on the optical elements at 12.661 keV and 4 keV. The vertical divergence of the photon source is the largest in the whole energy range. All distances are in mm.

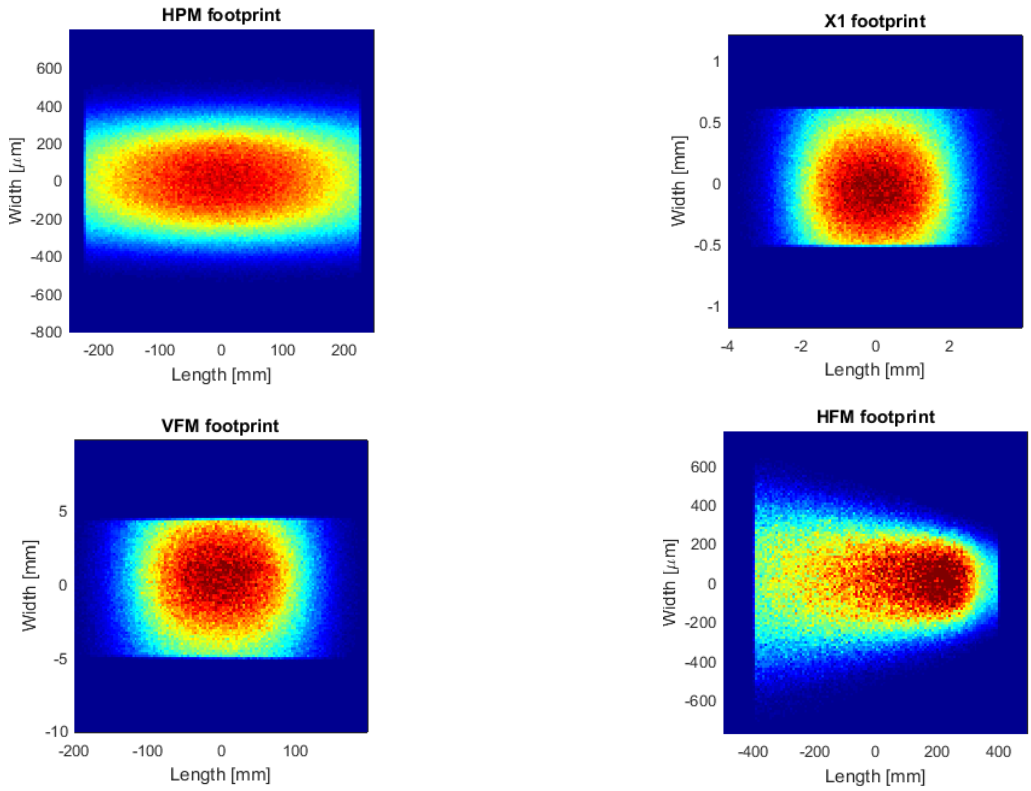

Figure 22. Footprints of the beam at 12.661 keV on the surfaces of all the reflecting mirrors (HPM, VFM and HFM) and the first crystal of the monochromator (X1). X1 is assumed to use the Si(111) reflection and has a grazing incidence of 9.063 deg. Note that the power footprint on the X1 is much larger than the beam footprint.

6.5 Variable beam size at sample

A variable beam size in both vertical and horizontal directions is required to optimize the beamline to the large variety of crystal morphology and MX methods. The proposed solutions are different for both directions, given the different beam size and divergence.

6.5.1 Horizontal adjustment

The horizontal beam size at focal position is ~3 μm, and the divergence is ~1.1 μrad. The beam is trimmed to lower sizes by means of the Horizontal Secondary Source slit (HSS) at the expense of reducing the flux. To expand the beam size at the sample position, the mirrors will be defocused. No beam striations are expected due to the large horizontal emittance of the photon source.

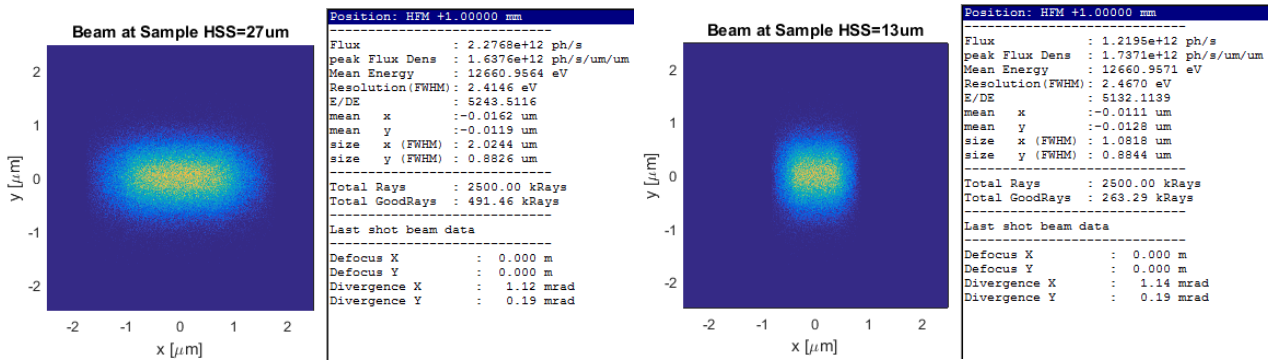

Figure 23. Beam spots at sample obtained by reducing the horizontal secondary source (HSS) slit. (*left*) beam reduced to 2×1 μm by closing the slits to 27 μm. (*right*) beam reduced to 1×1 μm by closing the slits to 13 μm.

6.5.2 Vertical defocusing

The beam can not be reduced to smaller sizes than the actual focus due to the absence of a vertical secondary source, and is not required by the scientific case. However, vertical expansion of the beam can be performed by two different methods.

The first beam expansion method is based on defocusing by increasing the bending radius of the VFM, so that the beam focus is pushed further downstream to the beamline axis and effectively increasing the beam size at the sample position. The method is inexpensive, but may produce an inhomogeneous beam spot due to the small vertical emittance of the source and the surface slope errors of the VFM. Moreover, the beam will probably need to require adjustment as it may move when adjusting the bending motors.

A second method to expand vertically the beam consists in introducing compound refractive lenses (CRLs) close to the sample position, so that the beam is focused upstream the sample position at a distance. The new position of the focus depends upon the energy (via the dependence of the real part of the refractive index of the lens material) and the radius of curvature. Given the low working energies of the beamline, the lenses should be made of Beryllium to avoid losses in flux due to low transmission. Assuming N plano-concave spherical surfaces with a focal distance $R/(2N\delta)$, placed at a distance u (>0) from the sample position and focusing at a distance v, the size of the expanded beam $\Delta\Sigma_y$ is given by

$$\Delta\Sigma_y = \sqrt{\Sigma_y^2 + \left((v-u)\,\Sigma'_y\right)^2}$$

$$\frac{1}{v} = \frac{N\delta}{R_{CRL}} + \frac{1}{u} \qquad (7)$$

where Σ_y and Σ'_y are the vertical beam size and divergence at the sample position without defocusing. According to these expressions, the beam can be effectively defocused vertically by inserting an array of 4 bi-lenses at 0.4 m upstream the sample position, where the beam has a FWHM vertical beam size of only 80 μm (Figure 24). The beam can thus can be completely accepted and the flux is only reduced by the transmission factor of the beam across the Be material. (7)

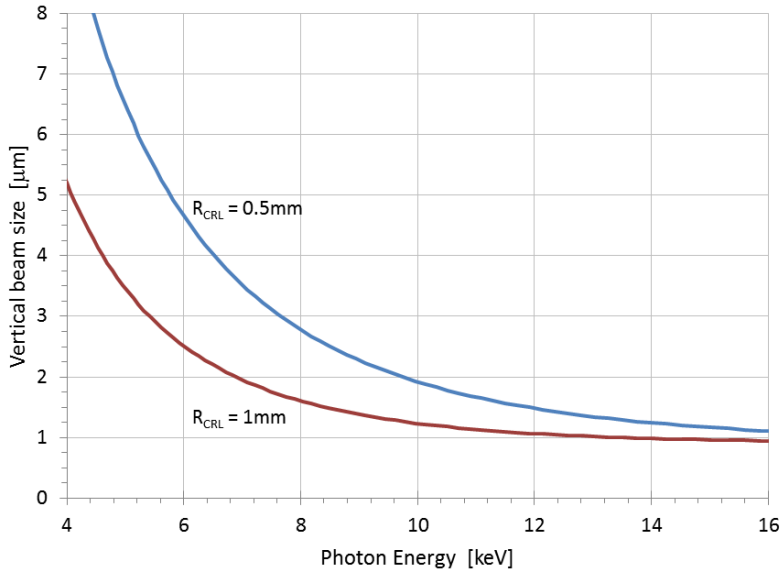

Figure 24. Vertical beam expansion produced by an array of 4 bi-concave beryllium lenses placed at 0.4 m from sample position, for two different radii. The beam may further expanded by introducing more lenses to the beam path or reducing the radius of curvature.

7 Power load on the optical elements

Two optical elements, the HPM and X1, are absorbing all the power passing through the front-end. The surface of the HPM is hit by the white beam passing through the front-end. Downstream to the mirror, the first crystal of the mono X1 receives the load of the remaining pink beam. The large amount of absorbed power induces a significant increase of the temperature and an expansion or contraction of the optical surface. The final temperature and shape of the surface depend on many parameters such as the power load, the geometry of the optical element, the cooling system, the thermal properties (conductivity, expansion) of the bulk material and the interfaces. To simulate the effect on the optical surface, a thermal finite element analysis (FEA) is required.

It is worth noting that in earlier stages of the design, the monochromator was placed as the first optical element of the beamline, and thus absorbing the white beam from the undulator. The first FEA models (not shown) displayed a temperature close to 200K, and an extremely large thermal bump. The current design avoids this problem by dividing the power load by the first crystal X1 and the HPM.

The X1 and HPM are assumed to be made of silicon crystal, and that the power is deposited on it. We are therefore disregarding the effect of the Rh coating stripe of the HPM and the multilayer grown on the crystal surface. Nevertheless, the thicknesses are less than 1 μm in both cases and therefore both the coating and the multilayer may be neglected for the thermal analysis. The optimized geometries of the X1 and HPM and their cooling systems are depicted in Figure 25.

Two scenarios are used in the FEA calculations, the working and worst conditions, according to section 1.4.

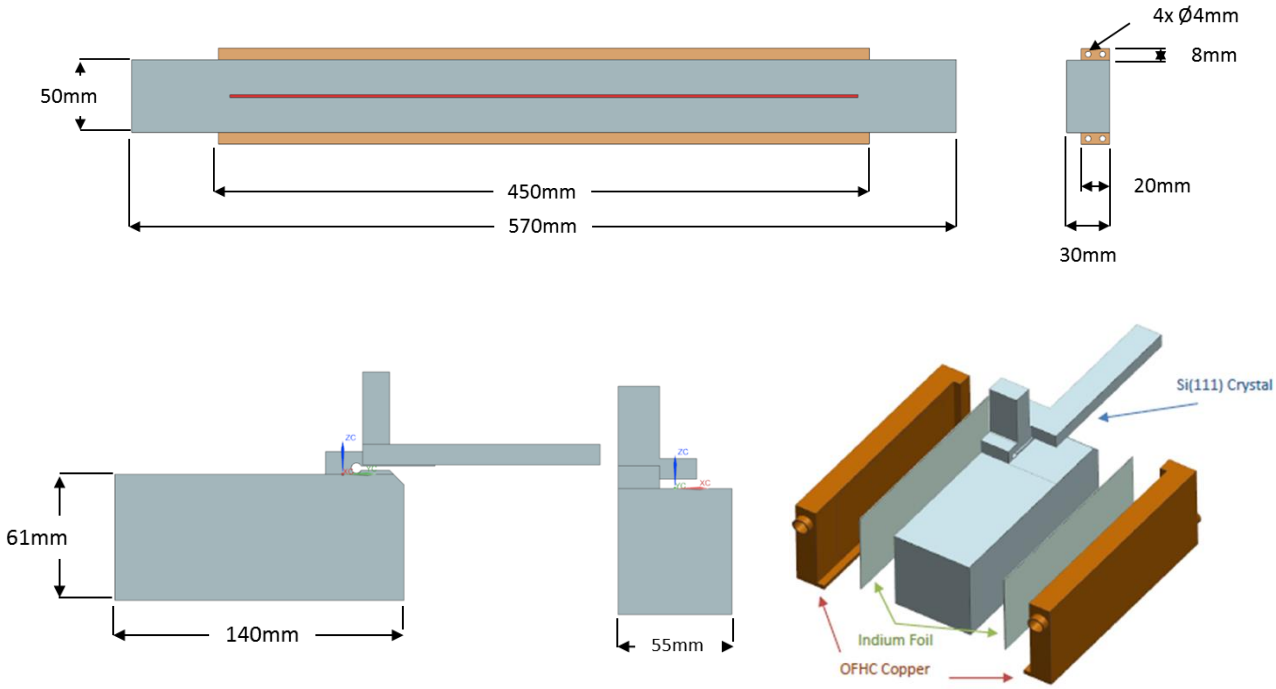

Figure 25. (*top*) Geometry of the HPM with the water cooling system. (bottom) Geometry of the channel-cut crystal and its cryocooling cooling. The LN_2 cooling is applied through the lateral surfaces of the crystal. The thermal conductivity between the mirror and the copper coolers is increased by using an indium-gallium layer, whereas the conductivity between the channel-cut block and the copper coolers is increased by using an indium foil.

7.1 Effect on the focusing properties of the thermal deformation in optical surfaces

A single-spot power footprint with a regular power density and a relatively constant thermal expansion coefficient within the temperature range of the surface induces a deformation that is approximated to a parabola (that is, a second-order Taylor approximation). In turn, the parabolic deformation can be approximated to a spherical deformation with radius R = $1/2a$, where a is the second order coefficient of the parabola. Using these approximations, the meridional and sagittal radii of curvature induced by the thermal load, $R_{Th,m}$ and $R_{Th,s}$ respectively, are proportional to the average along the optical surface of the second derivative of the deformation z of the crystal surface over the respective directions x (sagittal) and y (meridional) at the optical axes of the beamline y_0 and x_0 on the optical element surface, that is,

$$R_{Th,m} = \frac{1}{\langle \frac{\partial}{\partial x}\frac{\partial z}{\partial x} \rangle_{\Delta x,\, y_0}} \qquad (8)$$

$$R_{Th,s} = \frac{1}{\langle \frac{\partial}{\partial y}\frac{\partial z}{\partial y} \rangle_{\Delta y,\, x_0}}$$

The effect on the beam focusing distances of the induced thermal radii is calculated using the Codling equations below in both the meridional and the sagittal directions:

$$\frac{1}{p}+\frac{1}{q_e} = \frac{2}{\sin\alpha}\left(\frac{1}{R_m}+\frac{1}{R_{Th,m}}\right) = \frac{2}{R_{e,m}\sin\alpha}$$
$$\frac{1}{p}+\frac{1}{q_e} = 2\sin\alpha\left(\frac{1}{R_s}+\frac{1}{R_{Th,s}}\right) = \frac{2\sin\alpha}{R_{e,s}} \quad (9)$$

From equations (9) we derive that the meridional bending of an optical element will not be significantly influenced by the thermal meridional radius if $R_m << R_{m,Th}$, nor by the thermal sagittal radius if $R_m << R_{s,Th}\sin^2\alpha$. These rules also apply for crosstalk focusing, that is, for the unwanted influence of an optical element OE1 not designed to focus in a given direction on the focal distance of the mirror OE2 that was foreseen to focus in that direction, that is,

$$R_{OE1,m} \ll R_{OE2,s}\ \sin^2\alpha$$
$$R_{OE1,m} \ll R_{OE2,m} \quad (10)$$

7.2 Power load on the HPM

The power load on the horizontal prefocusing mirror is limited vertically by the front-end aperture, and horizontally by the limited acceptance of the mirror as defined by the length and the grazing incidence angle. The resulting power load is ≤430 W over the whole length of the mirror, which results in a moderate power density of ≤0.5 W/mm^2. These input conditions allow using a water cooling system applied at the side of the mirror.

	HPM Worst conditions	**HPM Working conditions**
Conditions		
Current in storage ring	400 mA	250 mA
Angular aperture (h×v)	0.099×0.100 mrad^2	0.099×0.150 mrad^2
Grazing incidence angle	4.5 mrad	4.5 mrad
Inputs FEA		
Absorbed power	429 W	360 W
Maximum power density	0.51 W/mm^2	0.319 W/mm^2
Coolant	turbulent water 23C Flow 0.76 l/min	turbulent water 23C Flow 0.76 l/min
Outputs FEA		
Maximum mirror Temperature	37.6 C	34.9 C
Minimum mirror Temperature	26.6 C	25.4 C
Induced meridional radius of curvature	9.404 km	7.998 km
Induced sagittal radius of curvature	87.72 m	146.4 m
Temperature increase of coolant	2.02 C	1.69 C

Table 11. Results of the thermal finite element analysis of the horizontal prefocusing mirror at worst and working conditions. Assumed distance of the mirror from source is 20.1 m.

The inputs and results of the FEA model, assuming the geometry given in Figure 25, are listed in Table 11. The temperature maps and the fitted radii of curvature are shown in Figure 26 and Figure 27 for the worst and working conditions. According to eq. (10), the thermal radius of the HPM is not influencing the vertical focusing of the beam by the VFM as $R_{VFM,m} << R_{HPM,s} \sin^2 \alpha$. In the meridional direction, the thermally-induced radius of curvature (~8 km) is longer than the nominal radius (~800 m, Table 9), so the effect can easily be corrected by adjusting the bending forces.

The acceptance of the optical surface of the mirror is smaller than the white beam size and the maximum aperture of the moveable slits. The fraction of the white beam passing through the front end but not accepted by the optical surface of the mirror must be absorbed by a heat absorber placed upstream to the HPM. In the absence of misalignments, the amount of power to dissipate is <350 W.

Similarly, there will be a part of the white beam that will not hit the mirror surface, but will continue along the beam path. This part of the beam has to be mirror absorbed by a second heat absorber placed upstream to the monochromator crystal. As in the case of the first absorber above, the power to dissipate is <350 W in the absence of misalignments.

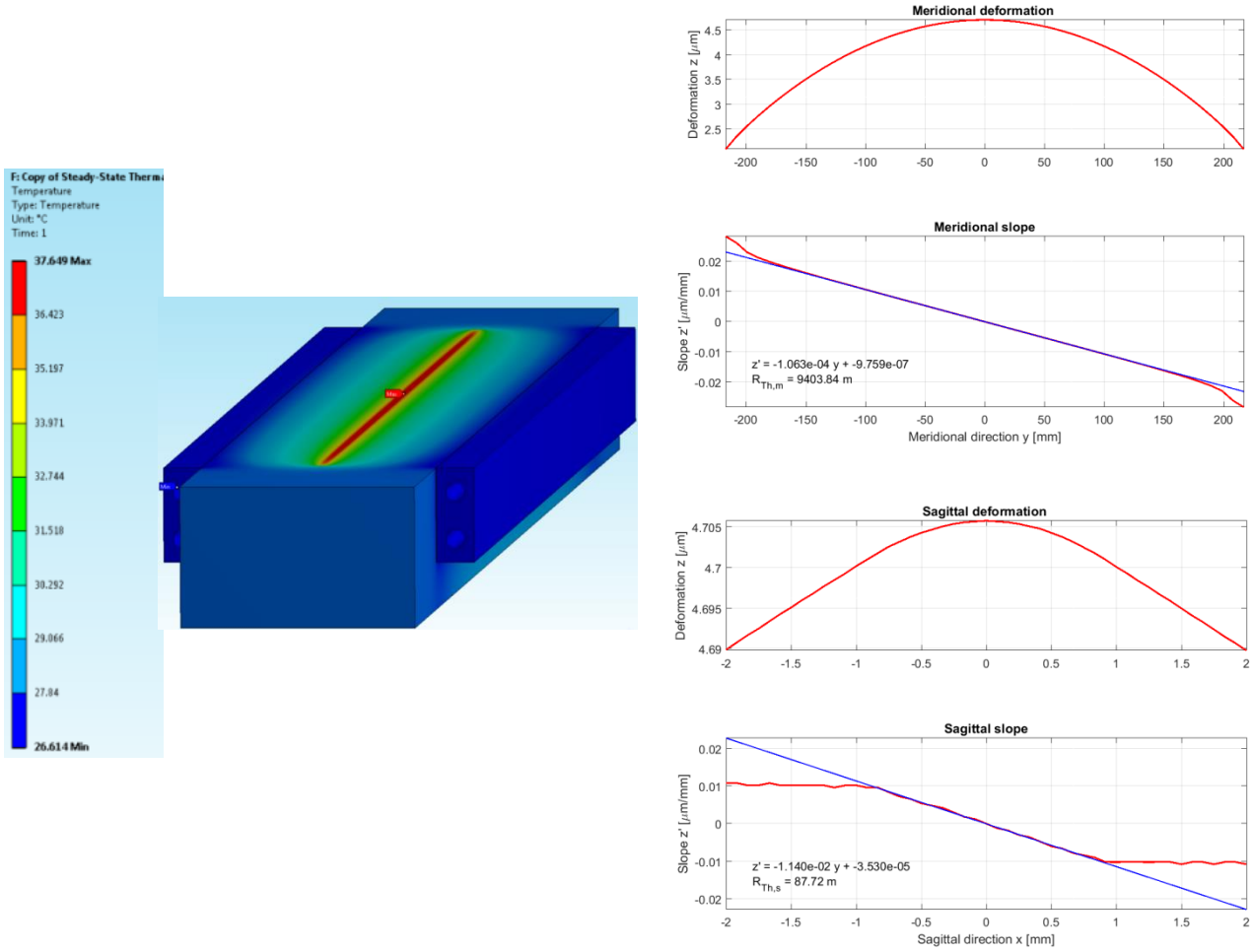

Figure 26. Results of the thermal FEA for the HPM at worst conditions. (*left*) Temperature map on the Horizontal Prefocusing Mirror. Temperatures range from 26.6 C to 37.6 C. (*right*) Meridional slope along the longitudinal direction of the horizontal prefocusing mirror.

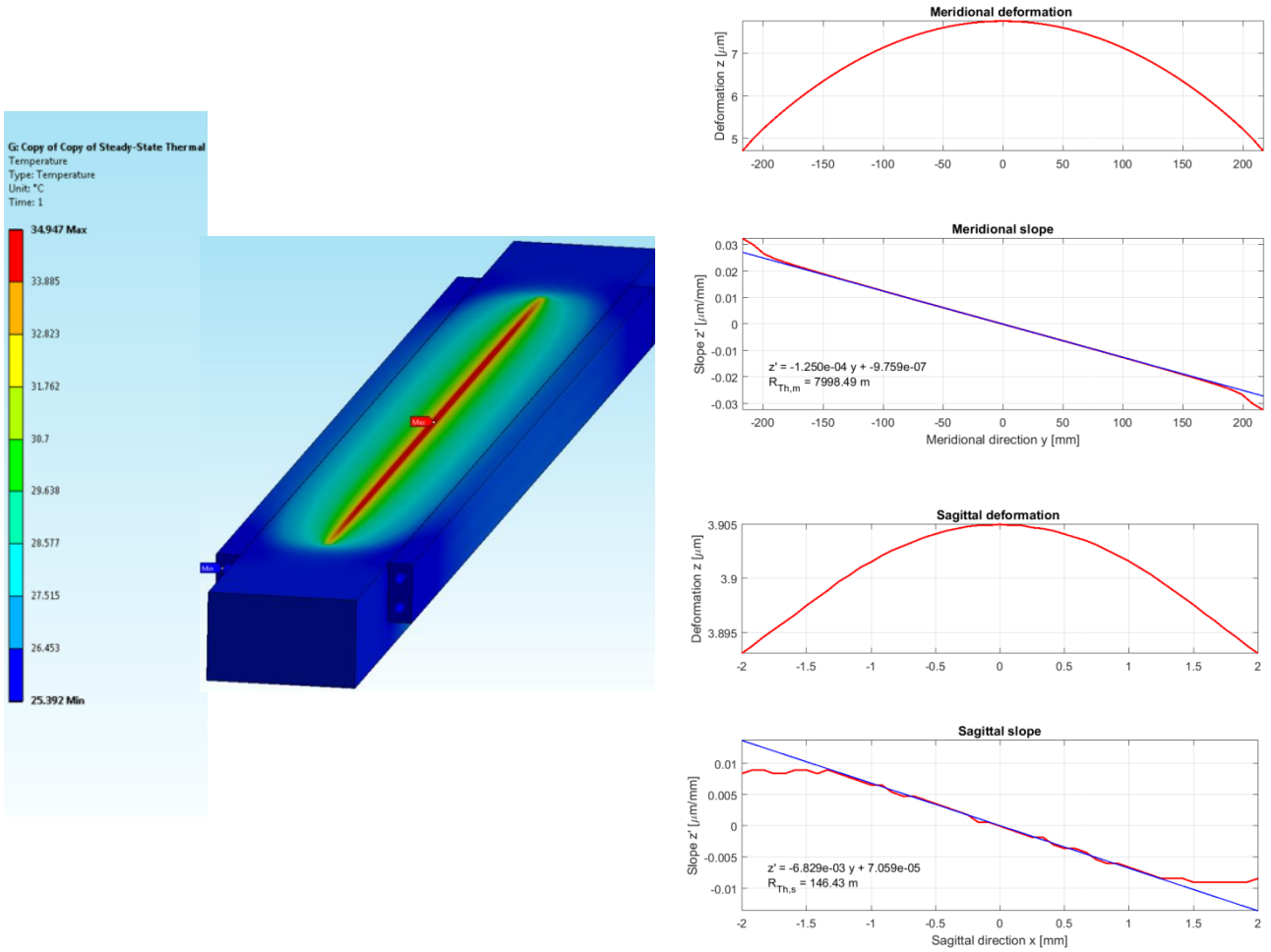

Figure 27. Results of the thermal FEA for the HPM at working conditions. (*left*) Temperature map on the Horizontal Prefocusing Mirror. Temperatures range from 25.4 C to 35 C. (*right*) Meridional slope along the longitudinal direction of the horizontal prefocusing mirror.

7.3 Power load on the first crystal of the monochromator

As in the case with the HPM, the power load on the first crystal of the monochromator is limited vertically by the front-end aperture and horizontally by the limited acceptance of the HPM. The resulting power load is below 300 W in all cases. The thermal load on the crystal is studied for 3 different Bragg angles: 29.7 deg and 9.064 deg (selected energies are 4 keV and 12.661 keV by using Si(111) reflection) and 1.5 deg (selected energy is ~12.6 keV by using a ML with $2d$~2 nm). The maximum power density on the crystal (31 W/mm^2) totally justifies the use of cryocooling, and is compatible with a design based on standard lateral copper coolers.

The inputs and results of the FEA model, assuming the geometry given in Figure 25, are listed in Table 12. The temperature maps and the fitted radii of curvature are shown in Figure 29 and Figure 28 for the worst and working conditions when using the Si(111) reflection at 4 keV and 12.661 keV, respectively. The deformations are not severely influencing the focal distances of the beam as per eq. (10), except for the case of worst conditions at 4 keV. In this

case, the maximum temperature reached is 153 K, which induces a meridional radius of curvature of ~-81 m (convex). This is an extreme case and it is not foreseen to be reached in the near future. Still, in this situation the front end moveable slits should be closed to reduce the total density, even though it would not reduce the power density.

Apart from this extreme case, the monochromator is not effectively influencing the focal distances of the beam and, thus, the horizontal and the vertical focal distances depend mainly on the meridional bending radii of the mirrors. The transversal dimensions of the beam appear to be decoupled, that is, the focusing of the beam in the horizontal direction depends solely on the HPM and HFM, whereas in the vertical direction depends on the VFM and, in the extreme mentioned above, the thermal radius of the first crystal of the monochromator.

The case of a multilayer at the worst case conditions and grazing incidence angle of 1.5 deg has also been considered (Figure 30). Due to the low angle, the power density of the footprint is very low and the induced thermal deformations are negligible.

	Mono X1 Worst conditions	**Mono X1 Working conditions**
Conditions		
Current in storage ring	400 mA	250 mA
Si(111) Angular aperture (h×v)	0.099×0.100 mrad^2	0.099×0.150 mrad^2
Multilayer Angular aperture (h×v)	0.050×0.100 mrad^2	-
Input FEA		
Absorbed power	273.9 W	235.5 W
Maximum absorbed power density	9.88 W/mm^2 (9.064 deg) 31.1 W/mm^2 (29.7 deg)	6.17 W/mm^2 (9.064 deg) 19.42 W/mm^2 (29.7 deg)
Coolant (effective cooling coef. *hcv*)	Liquid nitrogen 78K (3454 W/m^2/K)	Liquid nitrogen 78K (3454 W/m^2/K)
Output Si(111) (12.661 keV, 9.064 deg)		
Max T in crystal	105.4 K	95.1 K
Min T in crystal	81.6 K	81.0 K
Induced merid radius of curvature	3.213 km	5.893 km
Induced sagittal radius curvature	658.9 m	496.8 m
Output Si(111) (4 keV, 29.7 deg)		
Maximum Temperature	153.7 K	119.5 K
Minimum Temperature	81.5 K	80.9 K
Induced merid radius of curvature	-81.32 m	30.888 km
Induced sagittal radius curvature	-25.13 m	-315.5 m
Output Multilayer (12.6 keV, 1.5 deg)		
Maximum Temperature	84.3 K	-
Minimum Temperature	80.0 K	-
Induced merid radius of curvature	37.130 km	-
Induced sagittal radius curvature	1.545 km	-

Table 12. Results of the thermal finite element analysis of the first crystal of the monochromator at worst and working conditions, for two different Bragg angles corresponding to 12.661 keV (9.064deg) and 4 keV (29.7deg). The angular aperture of the beam for the multilayer has been reduced to the half to avoid the illumination of the rim of the surface. The assumed distance of the crystal from the source is 21.4 m.

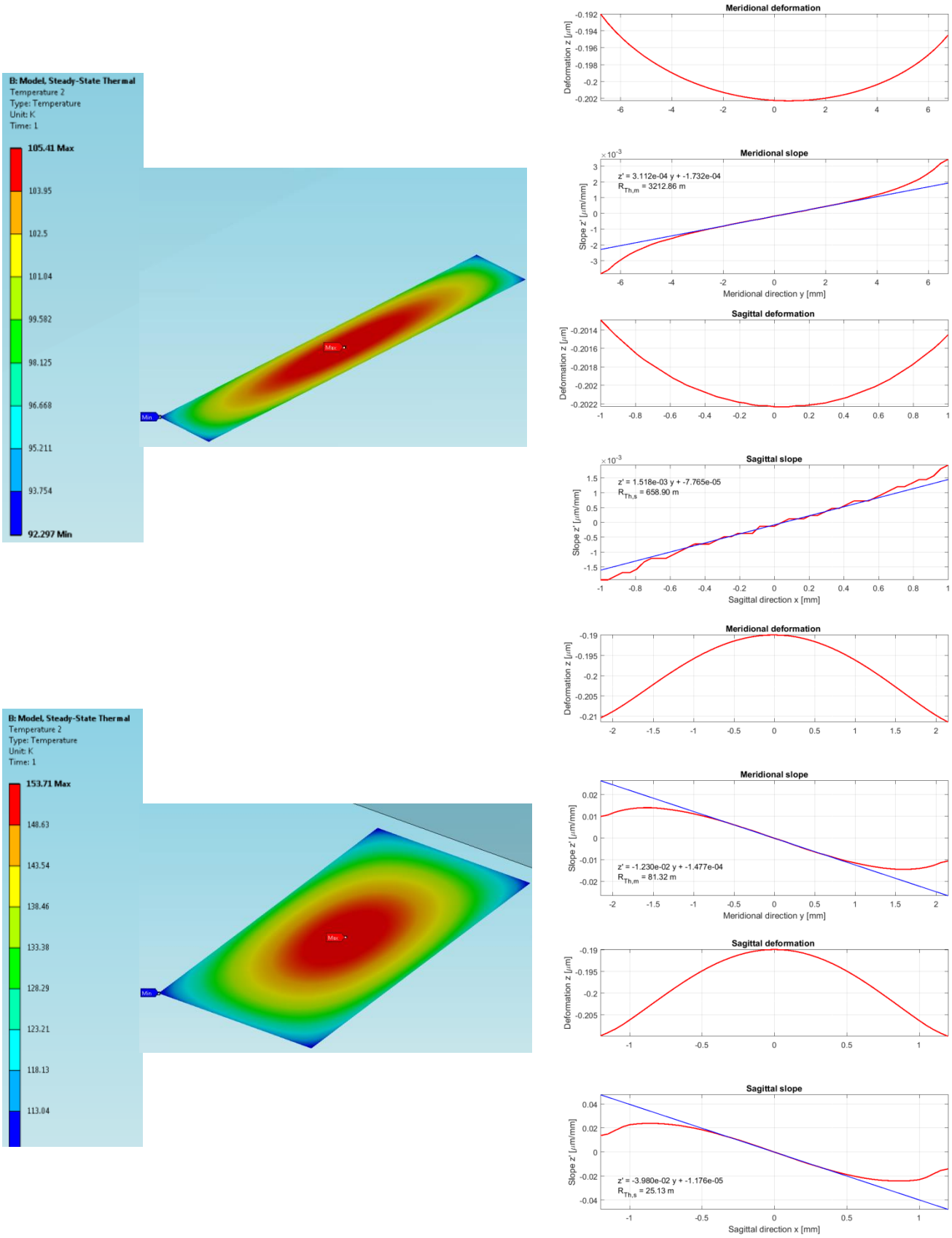

Figure 28. Results of the thermal FEA for the first crystal of the mono at **worst** conditions at 9.064 deg (*top*) and 29.7 deg (*bottom*). (*left side figures*) Temperature map on the exposed region on the first crystal. The temperatures range from 81 to 105K (9.064 deg) and from 108 to 153.7K (29.7 deg). (*right side figures*) Profiles of the meridional and sagittal deformation and slopes of the first crystal surface. The resulting radius of curvature $R_{Th,m/s}$ due to thermal effects in marked in the plot of the slope error. Due to the zero expansion point of Si at 129K, the monochromator shows a thermal hole at 9.064 deg, and a thermal bump at 29.7 deg.

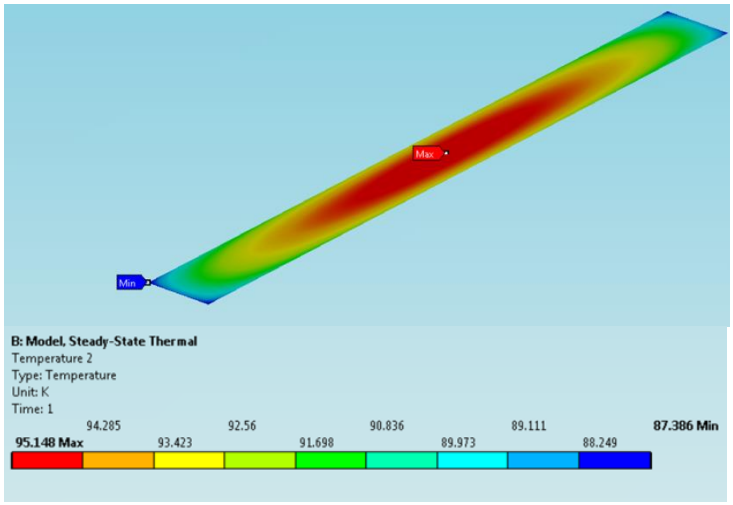

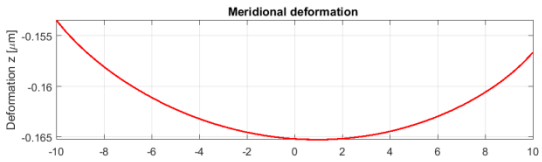

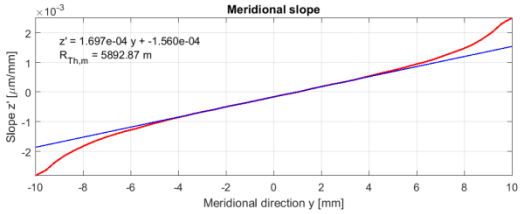

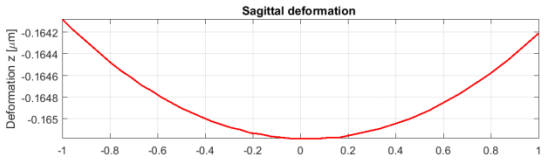

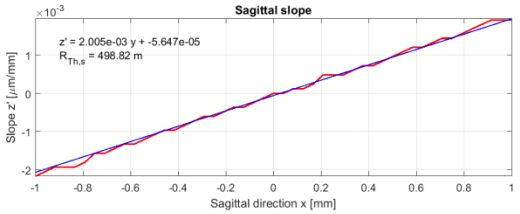

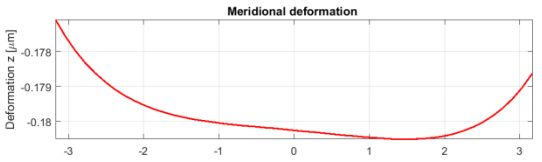

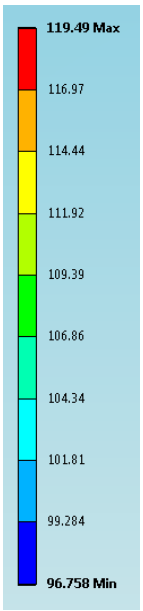

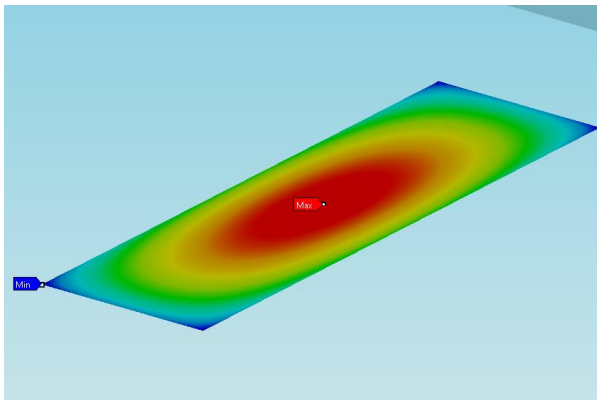

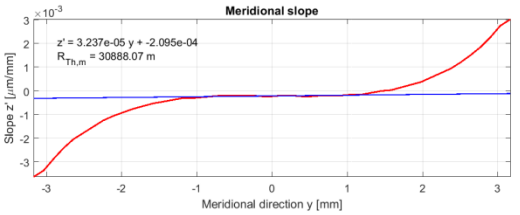

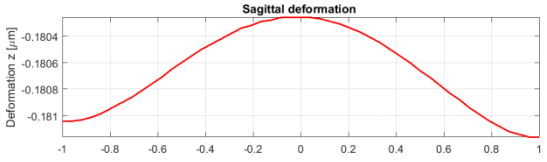

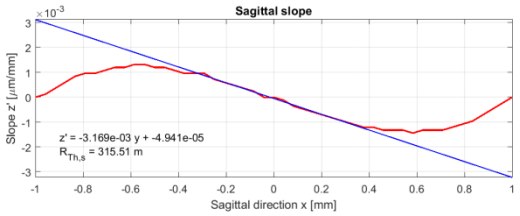

Figure 29. Results of the thermal FEA for the first crystal of the monochromator at **working** conditions at 9.064 deg (*top*) and 29.7 deg (*bottom*). (*left side figures*) Temperature maps on the exposed region on the first crystal. (*right side figures*) Profiles of the meridional and sagittal deformation and slopes of the first crystal surface. The resulting radius of curvature $R_{Th,m/s}$ due to thermal effects, calculated by equation () is marked in the plot of the slope error. Due to the zero expansion point of Si at 129K, the monochromator shows a thermal hole at 9.064 deg, and a thermal bump at 29.7 deg.

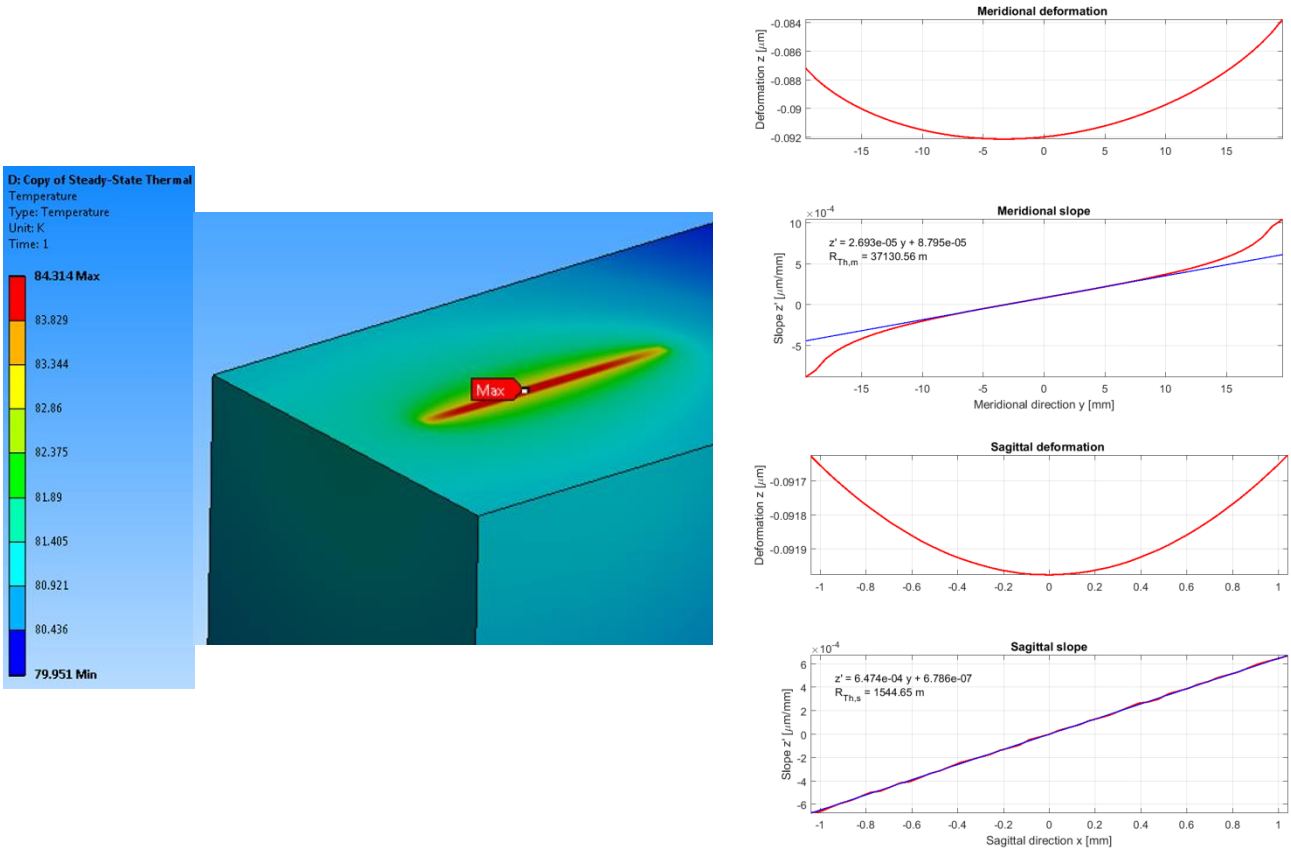

Figure 30. Results of the thermal FEA for the multilayer grown on the first crystal of the mono, at worst conditions except for the vertical beam divergence, which is reduced to the half (0.05 mrad) to avoid hitting the side of the crystal block. The grazing incidence angle is 1.5 deg, so that a multilayer with a period of 2 nm would diffract at 12.6 keV. (*left side figures*) Temperature map on the exposed region on the first crystal. The temperatures range from 80 to 84K. (*right side figures*) Profiles of the meridional and sagittal deformation and slopes. The effect of the thermal conductivity of the multilayer is not considered.

7.4 Correction of the optical effects of the power load

According to the results of the previous chapter, the thermal load effects on the HPM and the first crystal of the monochromator (X1) translate to the introduction of variable meridional and sagittal radii of curvature in each optical element. The optical effect of this thermal radius of curvature is a thermally-induced bending in the horizontal and vertical dimensions.

The effect of the thermal load, together with that of the slope errors of the mirrors, has been simulated by raytracing modeling with the ART package. The thermal deformations of the HPM and the X1 obtained by FEA have been introduced in the optical model of the beamline. In addition to this deformation, we introduce a slope error profile in the meridional direction for each mirror. The profiles are taken from the experimental data of the BL13-XALOC beamline mirrors, after the correction using the compensating actuators, as this is the most realistic model available (Figure 31). The slope error profiles have an RMS slope error value of 55 nrad and 83 nrad for the vertically (VFM) and the horizontally (HPM and HFM) reflecting mirrors

As expected from the values of the radii, the focal spots are bigger than the theoretical value, but can be corrected by a moderate defocusing Δq in either direction. The exception is the most critical case (worst case at 4 keV), in which a defocusing of 0.105 m must be applied.on the VFM. Nevertheless, this value is small compared to the nominal q value of the mirror, 1.743 m, so the mirror bender should be able to cope with the correction.

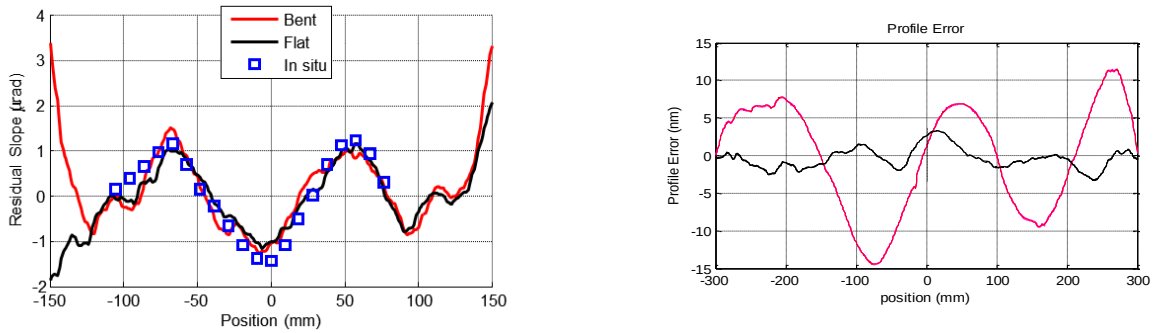

Figure 31. Meridional slope error profile assumed in the raytracing calculations. (*left*) Slope error profile for the VFM (red line). (*right*) Slope error profile for the HPM and HFM (black line). The profiles were measured at ALBA NOM from the VFM and the HFM mirrors of BL13-XALOC at ALBA synchrotron. The RMS values are 55 nrad and 83 mrad for the VFM and the HFM profiles, respectively. The length of the BL06-XAIRA mirrors not covered by these profiles (the outer 50mm and 100mm for the VFM and HFM) are considered flat.

	Beam size Not corrected	**Beam size Corrected**	**Focusing correction** Δq_h / Δq_v
HPM + X1 (9.064 deg, 12.661 keV)			
Worst conditions	4.8×2.4 μm²	3.1×0.90 μm²	2 / -5 mm
Working conditions	4.3×1.6 μm²	2.7×0.92 μm²	1 / -3 mm
HPM + X1 (29.7 deg, 4 keV)			
Worst conditions	4.6×59 μm²	2.5×1.9 μm²	1 / 105 mm
Working conditions	3.9×1.1 μm²	2.5×1.1 μm²	1.1 / 0 mm

Table 13. Beam size at sample position as modeled by raytracing, including the thermal deformations and the slope errors of the HPM and the X1 at the worst and working conditions for two different Bragg angles corresponding to 12.661 keV (9.064deg) and 4 keV (29.7deg). Corrected values are not accurately optimized.

Worst conditions, 12.661 keV

Working conditions, 12.661 keV

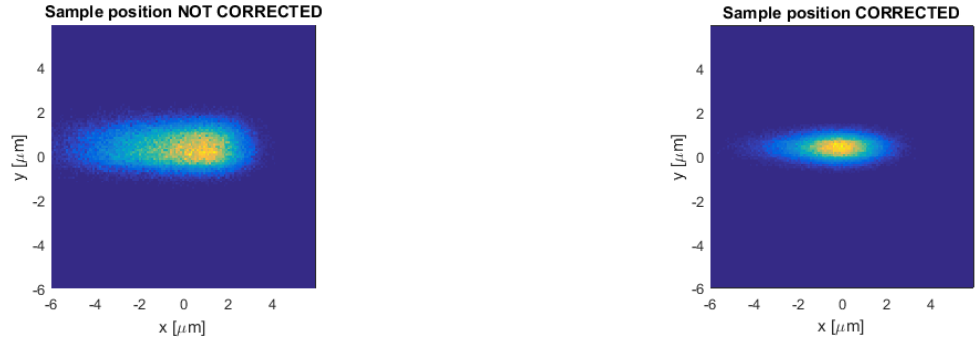

Worst conditions, 4 keV

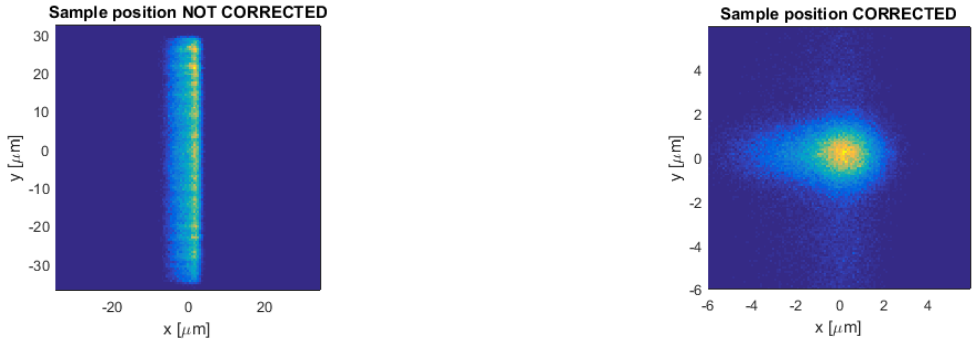

Working conditions, 4 keV

Figure 32. Beam spots at sample position including the thermal deformation of the HPM and X1, and the slope errors of the HPM, VFM and HFM. (*left*) Beam spots without refocusing the optics. (*right*) Beam spots after refocusing the VFM and/or the HFM. The variation of the focal distance $\Delta q_{h,v}$ is listed in Table 13 for all cases.

8 Vibrations

The stability of the beam is of paramount importance in a microfocus beamline. The requirements on the vibrational amplitudes for the different motions can be quantified using raytracing programs by simulating the beamline at slightly different alignment conditions in a single motion or adjustment, and collecting a set of the relevant characteristics of the beam to be monitored. A correlation matrix is built assuming a linear relation between the beamline adjustments and the beam characteristics. In the event that the matrix is squared, that is, there are as many beamline adjustments as beam parameters, the matrix can be inverted. The inverse matrix allows analyzing each movement of the beam in terms of adjustments of the beamline.

It is defined for XAIRA seven beam characteristics:

- Beam position at sample plane: Δx and Δy
- Beam orientation at sample position: $\Delta x'$ and $\Delta y'$.
- Beam size at sample position: σ_x and σ_y.
- Meridional position of the beam footprint at the HFM, u_{HFM}. This parameter is proportional to flux, as this is limited by the acceptance of the mirror

We also define seven critical adjustments that must be specified:

- Pitch of the HPM dP_{HPM}.
- Pitch and height (linear position along the surface normal) of the HFM: dP_{HFM} and dZ_{HFM}.
- Pitch and height (linear position along the surface normal) of the VFM: dP_{VFM} and dZ_{VFM}.
- Pitch and height (linear position along the surface normal) of the second crystal of the monochromator X2: dP_{X2} and dZ_{X2}.

The correlation matrix has been calculated using ART raytracing program:

$$\begin{pmatrix} \Delta x \\ \Delta y \\ \Delta x' \\ \Delta y' \\ \sigma_x \\ \sigma_y \\ u_{HFM} \end{pmatrix} = \begin{pmatrix} 0.3976 & 1.9785 & 0.911 & 0 & 0 & 0 & 0 \\ 0 & 0 & 0 & -3.4842 & 0.9465 & 0.1043 & -2.2567 \\ 1.7105 & 1.9633 & -0.124 & 0 & 0 & 0 & 6.6736 \\ 0 & 0 & 0 & -1.9981 & -0.4495 & 0.8690 & 0 \\ 0.1692 & -0.0257 & 0 & 0 & 0 & 0 & 0 \\ 0 & 0 & 0 & 0.0242 & -0.0145 & 0.031 & 0.4165 \\ 253.14 & -2.8435 & -3.9227 & 5.3838 & 1.6490 & 1.54687 & -14.844 \end{pmatrix} \begin{pmatrix} dP_{HPM} \\ dP_{HFM} \\ dZ_{HFM} \\ dP_{VFM} \\ dZ_{VFM} \\ dZ_{X2} \\ dP_{X2} \end{pmatrix}$$

where linear and angular magnitudes are expressed in μm and μrad, respectively. Assuming a general tolerance criterion of 10% of the nominal value for each magnitude, the correlation matrix leads allows calculating the maximum accepted amplitude. As the dependence in time of the beam characteristics is not considered, the misalignments, the vibrations and the motor resolutions can be treated using the same correlation matrix by only adjusting the tolerance criterion for each beam characteristic to the particular case.

The maximum vibration amplitudes allowed for each considered alignment are listed in Table 14. The critical beam characteristic is always the positioning of the beam, rather than beam size and beam divergence.

Motion/adjustment	Maximum amplitude	Critical beam characteristic
HPM pitch	0.75 μrad	Δx (<0.3 μm)
HFM pitch	0.15 μrad	Δx (<0.3 μm)
HFM height	0.3 μm	Δx (<0.3 μm)
VFM pitch	0.03 μrad	Δy (<0.1 μm)
VFM height	0.08 μm	Δy (<0.1 μm)
X2 pitch	0.04 μrad	Δy (<0.1 μm)
X2 height	1 μm	Δy (<0.1 μm)

Table 14. Maximum vibrational amplitudes allowed for each considered alignment in the correlation matrix.

9 Other optical elements

9.1 Diagnostics

The diagnostics system is based on fluorescence screens to control the beam profile and shape, and on diodes to monitor the photon intensity (Figure 33). All diagnostics intercepting the beam path must be retractable. The foreseen diagnostic elements are:

- **FS1**: White beam fluorescence screen, placed in principle before the HPM. FS1 could be placed downstream the HPM and upstream the monochromator provided that the monochromator and/or the HPM were slightly moved to install the fluorescence screen in between.
- **FS2**: Monochromatic beam fluorescence screen, just after the horizontal secondary source (HSS) slit.
- **FS3**: Fluorescence screen in the experimental hutch, upstream the KB system (HFM and VFM).
- **FS4**: Fluorescence screen in the experimental hutch, downstream the KB system.
- **FS5**: Fluorescence screen at the sample position.

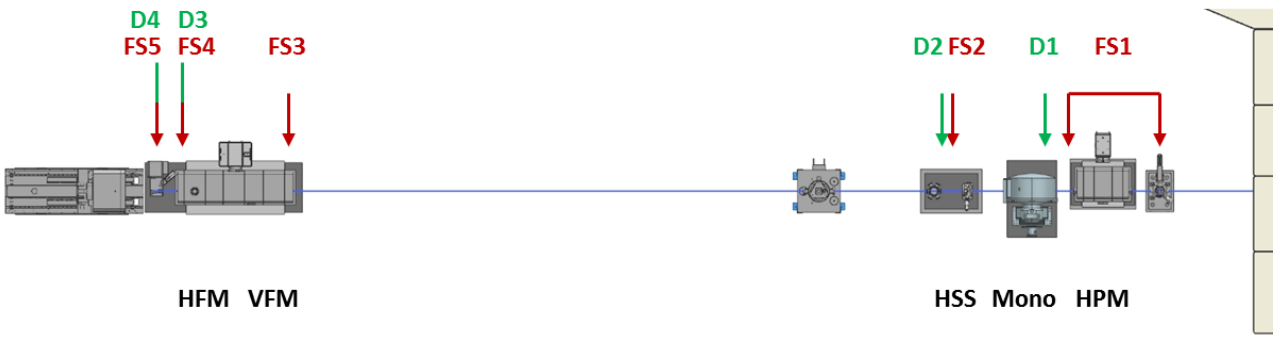

Figure 33. Position of the beam diagnostic elements. Fluorescence screens (FS) are marked in red, intensity monitors (D) are marked in green.

- **D1**: Intensity monitor, detecting the Compton and elastic scattering (proportional to the incoming photon flux) from the first surface of the monochromator. Does not intercept the beam.
- **D2**: Intensity monitor after HSS slit .
- **D3**: Intensity monitor after the KB system.
- **D4**: Intensity monitor at the sample position.

9.2 Slits and apertures

A simple scheme of slits and apertures is foreseen to figure the beam (Figure 34). The vertical beam divergence can be reduced by the front-end masks and the apertures VA1 and VA2. The horizontal beam divergence can be reduced by the front-end masks and the aperture HA1. The horizontal beam size can be adjusted at the focal point of the HPM, where the horizontal secondary slit (HSS) is installed.

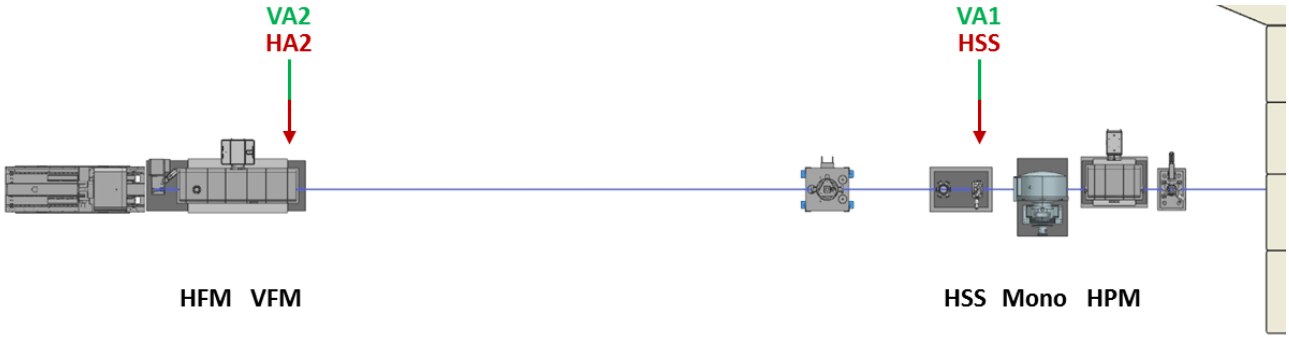

Figure 34. Position of slits and apertures. Horizontal slits and apertures are marked in red, whereas vertical slits are marked in green. Apertures and collimators are foreseen close to the sample position (not shown).

10 Safety

The optical hutch has to be designed to enclose the white beam from the undulator as well as the gas bremsstrahlung from the storage. The radiological protection elements, the 1st and 2nd bremsstrahlung stops, must be placed such that the experimental hutch can be designed to protect from the monochromatic beam, apart from the residual gas bremsstrahlung scattered by the elements in the optical hutch.

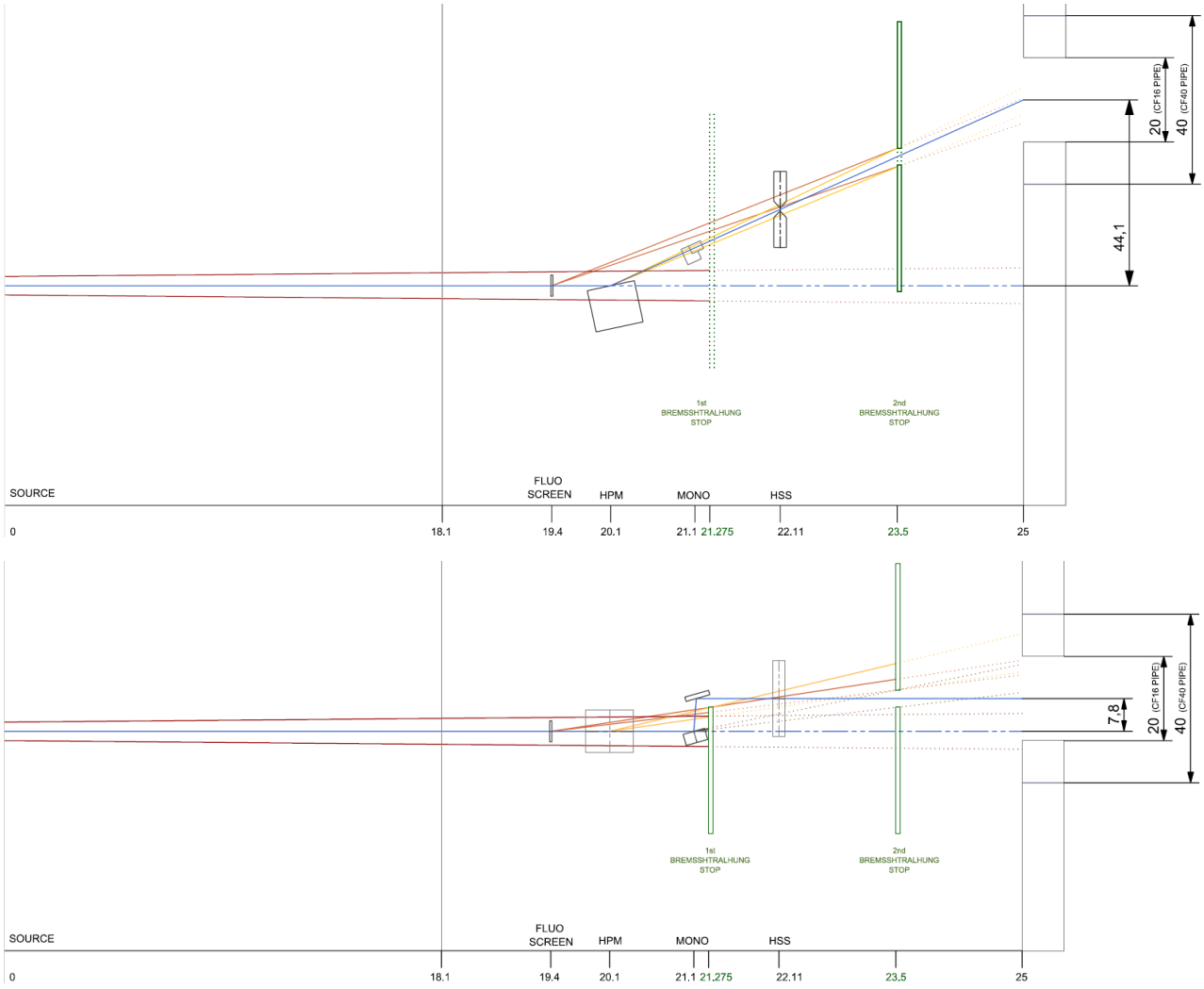

Figure 35. Limit ray tracing of the experimental hutch.

A first step is done by calculating the limit ray tracing of the optical hutch (Figure 35). Several assumptions have been done to ensure the validity of the model:

- A natural cross-section of 0.75 mrad divergence from the source must be covered in both transversal dimensions.
- To ease the calculations, a small back wall hole is assumed, only 20mm diameter
- A second scatterer is assumed upstream the HPM (a fluorescence screen)

We note that the small gap between the crystal surfaces of the channel-cut monochromator, 4.5 mm is fully compatible with the installation of the radiological safety elements in the optical hutch. Still, the complete validation of this scheme by Montecarlo models of radiation, together with the thicknesses of the lead hutches is to be defined in a later stage.

11 Hutches

Current design of the hutches layout is depicted in Figure 36. The total area of the BL06-XAIRA beamline, including spaces in between the hutches is 130 m^2. The lay out takes into account the area required to build the neighbor beamlines BL05 and BL07, fed by the adjacent bending magnet ports.

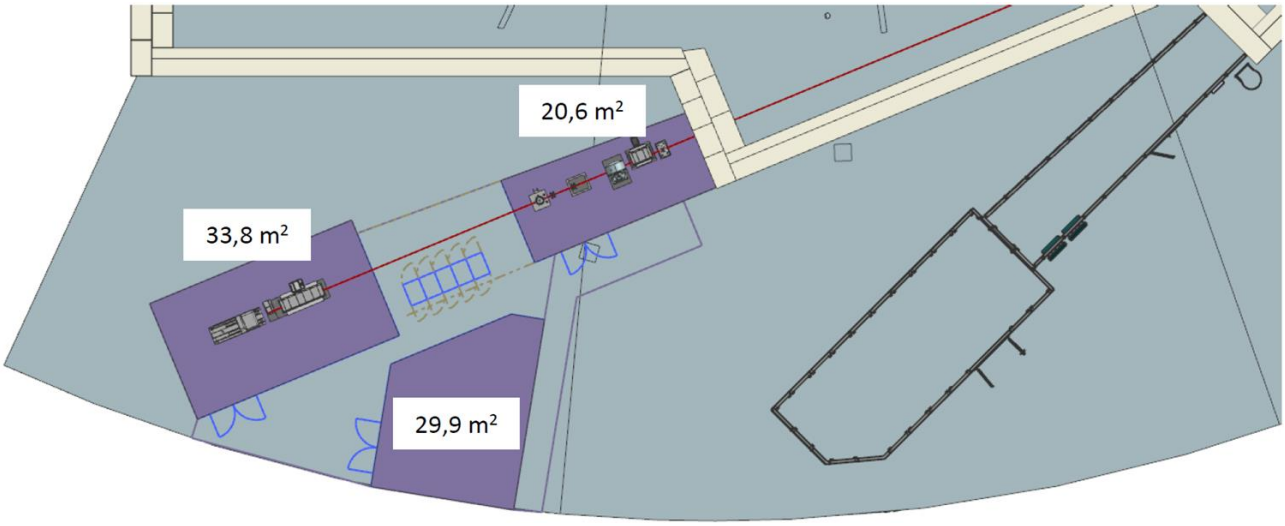

Figure 36. Schematic lay out of the hutches.

12 Services

12.1 Vacuum

The beamline after the last element of the front end, the trigger unit placed just after the tunnel shielding wall, is divided in 10 vacuum sectors (Figure 37). All the vacuum sectors of the optics hutch (VS1-VS6) are in ultra-high vacuum (~10^{-9} mbar). Vacuum sectors of the experimental hutch (VS7-VS9) are foreseen to be under high vacuum (~10^{-6} mbar). The transition between levels of vacuum is foreseen to be done by differential vacuum using the flight tube between hutches. The flight tube is around 5 m and, from the point of view of vacuum should have the smallest diameter compatible with the safe operation of the beamline.

No vacuum windows are employed due to the low energies in the hard X-ray range that the beamline must cover (4 keV). A detailed vacuum study is required in the near future to validate this scheme.

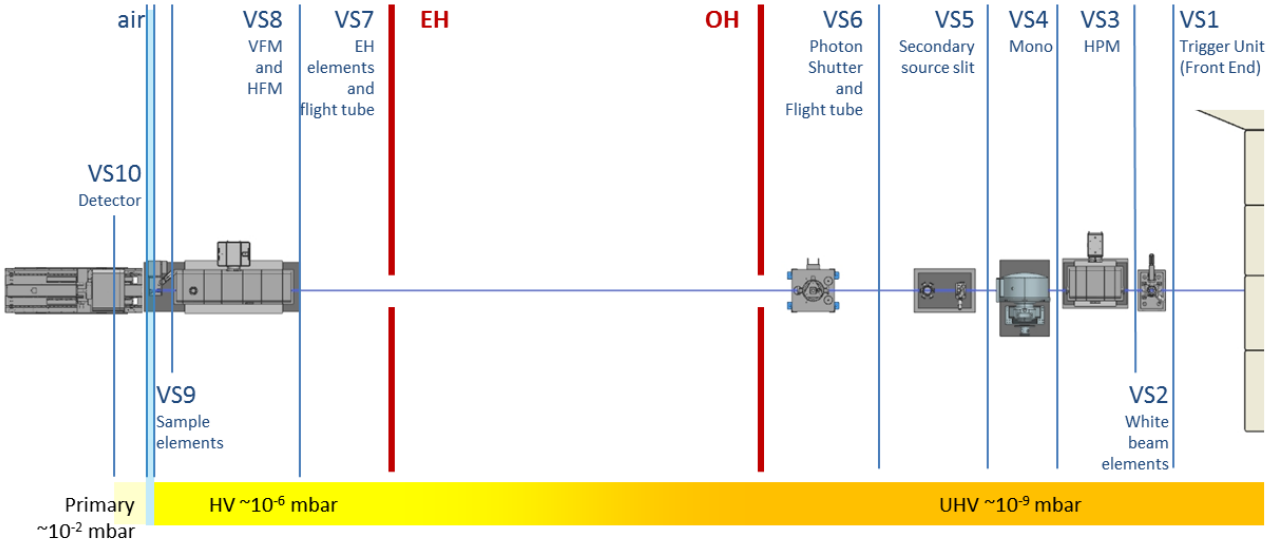

Figure 37. Vacuum scheme of the beamline.

12.2 Fluids

The fluid services in the optical hutch must include:

- **Dry compressed air**: to operate the valves, the photon shutter and other pneumatically actuated devices.
- **Pure** (4.0) **nitrogen gas**: For venting vacuum chambers.
- **Liquid nitrogen**: To cryocool the monochromator.
- **Cooling water**: to evacuate heat from the HPM, attenuator and white beam diagnostics

The fluid services in the experimental hutch must include:

- **Dry compressed air**: *id*.
- **Pure** (4.0) **nitrogen gas**: *id*.
- **Liquid nitrogen**: To refill the sample changer and the cryostream Dewars.
- **Helium** at room temperature: to refill the He cone placed between the sample and the detector.
- **Primary vacuum line:** To allow locating the primary pumps outside the hutch. This strategy reduces the vibrations and the noise level of the experimental hutch.

13 References

[1] S. M. Gruner and E. E. Lattman, “Biostructural Science Inspired by Next-Generation X-Ray Sources,” *Annu. Rev. Biophys.*, pp. 33–51, 2015.

[2] J. R. Helliwell and E. P. Mitchell, “Synchrotron radiation macromolecular crystallography: science and spin-offs,” *IUCrJ*, vol. 2, no. 2013, pp. 283–291, 2015.

[3] R. L. Owen, J. Juanhuix, and M. Fuchs, “Current advances in synchrotron radiation instrumentation for MX experiments,” *Arch. Biochem. Biophys.*, vol. 602, 2016.

[4] M. R. Fuchs *et al.*, “NSLS-II Biomedical Beamlines for Macromolecular Crystallography, FMX and AMX, and for X-ray Scattering, LIX: Current Developments,” *J. Phys. Conf. Ser.*, vol. 493, p. 12021, 2014.

[5] Q. Liu and W. A. Hendrickson, “Crystallographic phasing from weak anomalous signals,” *Curr. Opin. Struct. Biol.*, vol. 34, 2015.

[6] Q. Liu *et al.*, “Multi-crystal native SAD analysis at 6 keV,” *Acta Crystallogr. Sect. D Biol. Crystallogr.*, vol. 70, no. 10, pp. 2544–2557, 2014.

[7] Q. Q. Liu, Q. Q. Liu, and W. a. Hendrickson, “Robust structural analysis of native biological macromolecules from multi-crystal anomalous diffraction data,” *Acta Crystallogr. Sect. D Biol. Crystallogr.*, vol. 69, no. 7, pp. 1314–1332, 2013.

[8] T. Senda, “On the influence of crystal size and wavelength on native SAD phasing research papers,” pp. 728–741, 2016.

[9] I. Melnikov *et al.*, “Fast iodide-SAD phasing for high-throughput membrane protein structure determination,” *Sci. Adv.*, vol. 3, no. 5, p. e1602952, 2017.

[10] G. Bunkóczi *et al.*, “Macromolecular X-ray structure determination using weak, single-wavelength anomalous data,” *Nat. Methods*, vol. 12, no. 2, pp. 127–130, 2014.

[11] A. Wagner, R. Duman, K. Henderson, and V. Mykhaylyk, “In-vacuum long-wavelength macromolecular crystallography,” *Acta Crystallogr. Sect. D Struct. Biol.*, vol. 72, no. 3, pp. 430–439, 2016.

[12] J. Nicolas, A. Barla, and J. Juanhuix, “The Alba ray tracing code: ART,” in *Proceedings of SPIE - The International Society for Optical Engineering*, 2013, vol. 8848.

[13] M. R. Fuchs *et al.*, “NSLS-II biomedical beamlines for micro-crystallography, FMX, and for highly automated crystallography, AMX: New opportunities for advanced data collection,” in *AIP Conference Proceedings*, 2016, vol. 1741.

[14] a M. Deacon, T. Appleby, D. H. Bilderback, S. E. Ealick, E. Fontes, and D. J. Thiel, “Protein crystallography using a multilayer monochromator.,” *J. Synchrotron Radiat.*, vol. 5, no. Pt 3, pp. 494–6, 1998.

[15] D. J. Butler and J. H. Kelly, “In-House design of the new Double Multilayer Monochromator (DMM) for beamline VMXi,” in *MEDSI2016*, 2016.

[16] A. Khounsary *et al.*, “Development of a multilayer monochromator system for the BioCAT beamline,” vol. 9963, p. 99630W, 2016.

[17] H. Jiang *et al.*, “Structural characterization and low-temperature properties of Ru/C multilayer monochromators with different periodic thicknesses,” *J. Synchrotron Radiat.*, vol. 22, no. 6, pp. 1379–1385, 2015.

[18] Y. Liu, Q. Huang, H. Jiang, Y. Yang, Z. Zhang, and Z. Wang, “Structure of Ru/B $_4$ C multilayer for high flux monochromator application,” vol. 9963, p. 99630H, 2016.

[19] D. L. Windt, “IMD—Software for modeling the optical properties of multilayer films,” *Comput. Phys.*, vol. 12, no. 4, p. 360, 1998.

[20] S. Narayanan, A. Sandy, D. Shu, M. Sprung, C. Preissner, and J. Sullivan, “Design and performance of an ultra-high-vacuum-compatible artificial channel-cut monochromator,” *J. Synchrotron Radiat.*, vol. 15, no. 1, pp. 12–18, 2008.

[21] J. Juanhuix *et al.*, “Developments in optics and performance at BL13-XALOC, the macromolecular crystallography beamline at the Alba Synchrotron,” *J. Synchrotron Radiat.*, vol. 21, no. 4, pp. 679–689, 2014.
[22] J. Nicolas, C. Ruget, and C. Colldelram, “Optics and mechanics of mirror benders.”
[23] S. G. Alcock, I. Nistea, J. P. Sutter, and K. Sawhney, “Characterization of a next-generation piezo bimorph X-ray mirror for synchrotron beamlines,” pp. 10–15, 2015.
[24] C. Colldelram *et al.*, “The Nanobender : a new X-ray mirror bender with nanometer figure correction,” in *Proceeding of MEDSI*, 2016, pp. 413–419.